

Variability of the X-ray obscuring wind in Mrk 335 with XMM-Newton/RGS

DANIELE ROGANTINI ^{1,2} ERIN KARA ² LUIGI C. GALLO ³ S. KOMOSSA ⁴ PETER KOSEC ⁵ DAN WILKINS ⁶
EHUD BEHAR ⁷ JOHEEN CHAKRABORTY ² DIRK GRUPE ⁸ MISSAGH MEHDIPOUR ⁹ CHRISTOS PANAGIOTOU ²
CIRO PINTO ¹⁰ AND IRINA ZHURAVLEVA ¹

¹*Department of Astronomy and Astrophysics, University of Chicago, Chicago, IL 60637, USA*

²*MIT Kavli Institute for Astrophysics and Space Research, Massachusetts Institute of Technology, Cambridge, MA 02139, USA*

³*Department of Astronomy and Physics, Saint Mary's University, Halifax, NS, Canada*

⁴*Max-Planck-Institut für Radioastronomie, Auf dem Hügel 69, D-53121 Bonn, Germany*

⁵*Center for Astrophysics | Harvard & Smithsonian, Cambridge, MA, USA*

⁶*Department of Astronomy, The Ohio State University, Columbus, OH, USA*

⁷*Department of Physics, Technion, Haifa 32000, Israel*

⁸*Department of Physics, Geology, & Engineering Technology, Northern Kentucky University, Highland Heights, KY, USA*

⁹*Department of Astronomy, University of Michigan, Ann Arbor, MI, USA*

¹⁰*INAF – IASF Palermo, Via Ugo La Malfa 153, I-90146 Palermo, Italy*

ABSTRACT

Transient X-ray obscuration in Seyfert 1 galaxies is thought to arise from clumpy accretion-disk winds near the broad-line region (BLR), but the wind structure and its short-timescale variability are difficult to measure because high-resolution spectra are often suppressed during deep low states. We analyse a coordinated XMM-Newton/NuSTAR campaign on Mrk 335 in June 2021, complemented by long-term *Swift* monitoring, which captured the source in an intermediate-flux state that preserves strong RGS absorption features. We first model the broadband spectral energy distribution to determine the ionising continuum and then perform self-consistent photoionisation modelling of the RGS spectra. The stacked RGS spectrum requires three photoionised absorbers with time-averaged $\log \xi \simeq 3.63$, 3.10, and 2.01 and outflow velocities $|v_{\text{out}}| \simeq 5820$, 3210, and 2140 km s⁻¹. Their properties are broadly consistent with the three-phase obscurer reported in the 2009 intermediate state, indicating recurring multi-phase obscuration over decade timescales. Using five consecutive RGS observations, we track the wind evolution on day timescales and find strong variability in column density and ionisation in all phases, together with smaller but coherent changes in outflow velocity. During a flare, the low-ionisation phase shows an extreme drop in N_{H} , and the subsequent epoch exhibits an increase in outflow velocity in all phases, consistent with rapid restructuring and possible radiative acceleration in a clumpy wind. The high-ionisation phase responds most directly to changes in the ionising luminosity, while the lowest-ionisation phase shows at most a delayed response. Order-of-magnitude constraints place the obscurer at BLR scales ($\sim 10^3$ – $10^5 R_{\text{g}}$), and simple continuity arguments suggest kinetic power that can reach the percent level of L_{bol} for plausible estimates of geometry and clumpiness.

Keywords: High Energy astrophysics (739)

1. INTRODUCTION

Active galactic nuclei (AGN) are among the most variable persistent sources in the Universe, exhibiting dramatic flux changes across a broad range of timescales and wavelengths (E. Kara & J. García 2025). The most pronounced variability often occurs in the X-ray band, where the flux can vary by nearly two orders of magnitude within just a few weeks (G. Ponti et al. 2012; S. Komossa et al. 2026). This variability may be driven by transient absorption events caused by clouds transiting the line of sight (J. S. Kaastra et al. 2014; S. Komossa et al. 2020; L. C. Gallo et al. 2021; E. Kara et al. 2021), or by intrinsic changes in the geometry or activity of the X-ray-emitting corona (E.

Kara et al. 2016; D. R. Wilkins et al. 2022). The competition between intrinsic variability and variable absorption presents a major observational challenge in interpreting AGN light curves and spectra, as these processes can operate simultaneously or mimic one another.

High-resolution X-ray spectroscopy is essential to disentangle absorption from intrinsic spectral changes, particularly through the detection of narrow absorption lines produced by ionised outflows. Narrow-line Seyfert 1 (NLS1) galaxies are especially valuable in this context due to their rapid and large-amplitude X-ray variability (L. Gallo 2018). More than half of Seyfert I galaxies exhibit rich soft X-ray spectra marked by absorption lines from warm absorbers, which span a wide range of ionisation parameters, form multiphase structures, and show outflow velocities of a few hundred up to a few thousand km/s (A. J. Blustin et al. 2005; S. Laha et al. 2021; L. C. Gallo et al. 2023). In addition, a handful of Seyfert I galaxies reveal absorption features from low-ionisation ultra-fast outflows (UFOs) (A. L. Longinotti et al. 2015; Y. Xu et al. 2023, 2024). These winds are of central interest because they may carry significant mass, momentum, and energy, thereby contributing to AGN feedback on their host galaxies.

In parallel, multiwavelength campaigns, most notably the *AGN STORM* series (G. De Rosa et al. 2015; E. Kara et al. 2021), have revealed episodes of strong, transient obscuration (“obscurers”) that can heavily suppress the soft X-ray emission and may represent a distinct form of mass ejection in AGN. These phenomena were first established in NGC 5548, where coordinated XMM-*Newton* and HST observations uncovered a newly emerging, partially covering outflow that strongly absorbed the soft X-ray continuum while imprinting deep, blueshifted UV absorption lines (J. S. Kaastra et al. 2014). Another well-known case is the NLS1 WPVS 007: as its X-ray flux became very weak, broad UV absorption emerged in FUSE spectra (K. M. Leighly et al. 2009, 2015). Such obscuring winds are markedly different from the commonly observed warm absorbers: they display higher column densities and velocities of several thousand km s⁻¹, and are launched from the inner broad-line region (BLR) rather than from the narrow-line region (NLR) (G. A. Kriss et al. 2019). The duration of these obscuration events varies widely, from days to months (e.g. Mrk 766, NGC 3227) to several years, as in the decade-long episode in NGC 5548 (M. Mehdipour et al. 2022). An increasing number of similar events have been reported in Seyfert 1 galaxies (e.g. A. G. Markowitz et al. 2014; J. Ebrero et al. 2016; R. Serafinelli et al. 2021; J. Mao et al. 2022a,b; Y. Wang et al. 2022; S. Grafton-Waters et al. 2023). A particularly well-observed example is NGC 6814, where a long XMM-*Newton* exposure captured a full obscurer eclipse lasting about 70 ks (L. C. Gallo et al. 2021; A. G. Gonzalez et al. 2024; B. Pottier et al. 2023; L. K. Pothier-Bogowski et al. 2025).

Key insights into obscuring winds were recently obtained by the *AGN STORM 2* campaign on Mrk 817, which caught the source during an unexpected obscuration phase (E. Kara et al. 2021). The obscuration was consistent with a dust-free, ionised, partially covering absorber located at the inner BLR (see also J. M. Miller et al. 2021). Four XMM-*Newton* observations were taken simultaneously with high-cadence HST monitoring; one of them coincided with a brief flux increase in April 2021, revealing a rich spectrum of narrow absorption lines. F. Zaidouni et al. (2024) detected a three-component photoionised wind with velocities of 4000–6000 km/s, consistent with UV absorption lines at the same velocities, confirming a common X-ray/UV origin. Subsequent NICER monitoring attributed the observed variability to combined changes in the obscurer column density (by more than an order of magnitude) and intrinsic continuum flux, indicating a clumpy disk wind whose transparency and ionisation evolve with luminosity (E. R. Partington et al. 2023).

Despite extensive observational efforts over the past decade, the physical nature of these obscurers remains poorly understood. They may represent discrete clumps lifted from the accretion disk by magnetic or radiative forces, or denser phases embedded within a continuous disk wind. Their connection to other classes of AGN winds, such as warm absorbers or ultra-fast outflows, is still unclear. The multiphase structure, dynamics, and global covering fraction of the obscuring gas are also uncertain. In addition, their optically thick nature often suppresses the soft X-ray band, limiting detailed spectral diagnostics with current observatories. Only in a few cases, such as Mrk 817 during temporary flux increases, has it been possible to probe the ionisation structure of the wind. However, these opportunities are sporadic and short-lived, preventing a systematic characterisation of obscurer properties and variability.

Our recent joint XMM-*Newton*/NuSTAR campaign of Mrk 335 opens a new window to study obscuration in unprecedented detail. Mrk 335 ($z = 0.0258$, $M_{\text{BH}} = 2.7 \times 10^7 M_{\odot}$; C. J. Grier et al. 2012) exhibits extreme X-ray variability driven by both absorption and changes in coronal geometry, making it a benchmark Seyfert 1 galaxy for studying accretion and outflow processes. Once among the brightest X-ray AGN (H. Tananbaum et al. 1978; S. Bianchi et al. 2001), Mrk 335 experienced a dramatic drop in flux in 2007 (D. Grupe et al. 2008), followed by a long transition phase and then a prolonged low-flux state punctuated by persistent flickering and episodic high-amplitude flares, sometimes

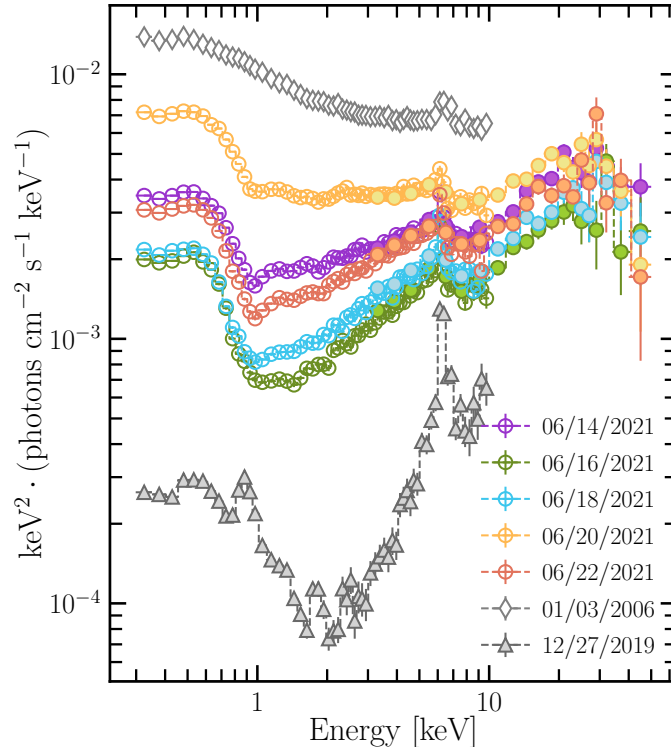


Figure 1. EPIC-pn and NuSTAR spectra of Mrk 335 obtained during the 2021 campaign. Open symbols show the EPIC-pn data (0.3–10 keV), while filled symbols indicate the simultaneous NuSTAR observations (3–50 keV). The coloured datasets correspond to the five 2021 campaign epochs, using the same colour scheme adopted for the light curves in Fig. 2. For comparison, we also show one of the lowest-flux EPIC-pn spectra ever observed (2019) and one of the highest-flux spectra (2006), just before the onset of the obscuration phase in Mrk 335.

brightening by a factor of ~ 50 on week-long timescales (D. Grupe et al. 2012; D. R. Wilkins et al. 2015; L. C. Gallo et al. 2019; S. Komossa et al. 2020; S. Tripathi et al. 2020). The source typically alternates between three flux regimes: a high state, in which the spectrum appears nearly unabsorbed as before 2007; a low state, in which the soft X-ray emission is almost completely suppressed; and an intermediate (“mid”) state, characterised by strong absorption lines from an obscuring wind (A. L. Longinotti et al. 2013; H. Liu et al. 2021). In June 2021, five consecutive XMM-*Newton* observations captured Mrk 335 in this intermediate state, providing an exceptional opportunity to resolve its rich absorption-line spectrum with the Reflection Grating Spectrometer (RGS) and to investigate in detail the variability and structure of its obscuring wind.

In Section 2, we describe the observations and data reduction. The analysis of the broadband spectral energy distribution (SED) is presented in Section 3, while Section 4.1 focuses on the high-resolution RGS spectra and the signatures of ionised outflows. The results on the variability and properties of the obscuring wind are discussed in Section 5 and summarised in Section 6. The spectral analysis was performed using the SPEX package (v3.08.01; J. S. Kaastra et al. 1996, 2020), using a hybrid statistical approach: the C -statistic for X-ray fitting and the standard χ^2 statistic for optical/UV data. Unless stated otherwise, all errors are quoted at the 1σ confidence level. Spectra were binned following the optimal binning algorithm of J. S. Kaastra & J. A. M. Bleeker (2016) to preserve spectral resolution while ensuring statistically robust fits.

2. OBSERVATIONS AND DATA REDUCTION

Mrk 335 was observed in June 2021 as part of a coordinated campaign consisting of five XMM-*Newton* observations obtained simultaneously with NuSTAR (PI: E. Kara; XMM-*Newton* proposal ObsID: 08427601). The observations span a total of eight days, providing broadband X-ray coverage across multiple epochs. The observation log is given in Table 1. This core program was complemented by an extensive *Swift* monitoring campaign (Swift Key Program, Cycle 15, PI: E. Kara; proposal number: 1518037), which places the joint XMM-*Newton*/NuSTAR exposures in a

Table 1. XMM-Newton, NuSTAR, and Swift observations of Mrk 335 in June 2021 including their gross exposure before filtering. We list only the Swift observations used for the SED modelling.

Epoch	Mission	ObsID	Start Date (UTC)	Exposure (ks)
XMM-Newton + NuSTAR				
1	XMM-Newton	0842761401	2021-06-14 06:03:03	93.9
	NuSTAR	60502006002	2021-06-14 03:51:07	51.4
2	XMM-Newton	0842760201	2021-06-16 05:52:43	93.9
	NuSTAR	60502006004	2021-06-16 05:46:11	47.5
3	XMM-Newton	0842761101	2021-06-18 05:40:24	94.0
	NuSTAR	60502006006	2021-06-18 06:01:09	47.3
4	XMM-Newton	0842761201	2021-06-20 05:34:44	93.9
	NuSTAR	60502006008	2021-06-20 06:21:10	49.4
5	XMM-Newton	0842761301	2021-06-22 05:42:46	93.0
	NuSTAR	60502006010	2021-06-22 05:06:09	43.1
Swift Monitoring				
–	Swift	00013544097	2021-06-13 02:28:35	1.68
–	Swift	00013544098	2021-06-14 03:53:35	0.89
–	Swift	00013544099	2021-06-15 03:58:36	0.85
–	Swift	00013544100	2021-06-16 13:18:36	0.95
–	Swift	00013544101	2021-06-17 14:43:36	0.86
–	Swift	00013544103	2021-06-18 08:19:35	1.03
–	Swift	00013544102	2021-06-19 00:09:35	0.99
–	Swift	00013544104	2021-06-20 16:09:50	0.44
–	Swift	00013544105	2021-06-21 22:09:36	1.00
–	Swift	00013544106	2021-06-23 01:31:35	0.47

broader temporal context. The observational setup of each instrument, together with the details of the data reduction and processing, is described below.

2.1. XMM-Newton

The campaign comprised five XMM-Newton observations performed over eight days between 2021-06-14 and 2021-06-22, each with a nominal exposure of ~ 94 ks.¹¹ We reduced the data using SAS v21.0 and the latest calibration files, including the energy-dependent correction described in F. Fürst (2022).

EPIC-pn (European Photon Imaging Camera; L. Strüder et al. 2001) was operated in Large Window mode. Periods of high background were excluded by rejecting intervals with count rate > 0.5 counts s^{-1} in a high-energy band (10–12 keV) using the #XMMEA_EP filter. A high-energy single-event light curve (PATTERN = 0, PI between 10–12 keV) was extracted over the full chip to identify flares. Source spectra were extracted from a circular region of radius $30''$ centred on the target. The background was extracted from a same-size circular region on the same CCD, selected from a nearby source-free area and avoiding chip edges where the instrumental Cu $K\alpha$ line is enhanced. Response matrices and ancillary response files were generated with `rmfgen` and `arfgen`, using the option `applyabsfluxcorr=yes` to apply the calibration correction tied to NuSTAR (see F. Fürst 2022). After filtering, the typical clean EPIC-pn exposure per observation is ~ 70 ks ($\approx 75\%$ of the nominal). The resulting EPIC-pn spectra from June 2021 are shown in Fig. 1, while the light curves and hardness ratios are presented in Fig. 2. The EPIC-pn observations taken in Large Window mode are affected by pileup. We checked the effect using the task `epaplot`. For each observation, we extract the source spectra from an annulus with the same outer radius $30''$ and an inner radius between $7.5''$ and $10''$ depending on the count rate and pileup intensity. Comparing the annular (pile-up-mitigated) spectra with the standard circular extractions, we find that pile-up affects the spectral shape only below 1 keV; above 1 keV the spectra are consistent within uncertainties for all epochs. Since we only use the EPIC pn in the energy band between 1.5 keV and 10 keV we

¹¹ Dates refer to the observation start times listed in Table 1.

use the spectra extracted by the circular region which guarantee the identical spectral fit and provide a higher signal to noise.

The RGS (Reflection Grating Spectrometers; J. W. den Herder et al. 2001) data were processed with the standard `rgsproc` pipeline. We excluded time intervals when the background count rate in CCD 9 exceeded $0.2 \text{ counts s}^{-1}$. In the spectral fits, we fitted the RGS1 and RGS2 spectra simultaneously over the 7–37 Å band.

The Optical Monitor (OM; K. O. Mason et al. 2001) was operated in image/fast mode. Throughout, only the UVW1 filter (212 nm) was used, with exposures of 4.4 ks each. Photometry was performed with `omichain` using a circular aperture of diameter $12''$ and standard settings.

2.2. NuSTAR

Mrk 335 was observed simultaneously with NuSTAR (F. A. Harrison et al. 2013), with exposures ranging from 43 to 51 ks. The data were reduced using the NuSTAR Data Analysis Software (`nustardas v1.9.2`) and the latest calibration files. Event lists from the two focal plane modules (FPMA and FPMB) were cleaned and calibrated with `nupipeline`, applying standard screening criteria. Periods of elevated background during passages through the South Atlantic Anomaly (SAA) were excluded using the default SAA filtering mode, and the depth correction was applied to reduce the internal high-energy background.

Source spectra were extracted from circular regions of radius $60''$ centred on the target, while background spectra were taken from nearby source-free regions of equal size on the same detector. The `nuproducts` task was used to generate the source and background spectra, together with the corresponding response files. In the spectral analysis, we used the 3–50 keV band and fitted FPMA and FPMB simultaneously, allowing for a cross-normalisation constant between the two modules. The resulting NuSTAR spectra are shown in Fig. 1, while the light curves are presented in Fig. 2.

2.3. Swift

During the June 2021 XMM-Newton campaign, *Swift* (N. Gehrels et al. 2004) monitored Mrk 335 with a cadence of one to two short snapshots per day, with occasional gaps due to gamma-ray burst triggers. The observations were obtained as part of a Cycle 15 Key Project, which started observing Mrk 335 on 2020 June 8. Individual visits typically had exposures of 0.5–1 ks.

The *Swift* X-ray Telescope (XRT; D. N. Burrows et al. 2005) was operated in photon counting mode. Light curves were generated using the online XRT data products tool (P. A. Evans et al. 2007, 2009). Standard processing was performed with `xrtpipeline`, which corrects for bad pixels, vignetting, and point-spread function effects to produce cleaned event files. XRT light curves in different energy bands were then extracted for each snapshot. The resulting *Swift* XRT light curve is presented in Fig. 2.

The *Swift* UV/Optical Telescope (UVOT; P. W. A. Roming et al. 2005) observed Mrk 335 with its six primary filters (*V*, *B*, *U*, *UVW1*, *UVM2*, *UVW2*) in end-weighted filter mode (0x224c), using a weighting scheme of 4:3:2:1:1:1 (from *UVW2* through *V*). Aperture photometry was performed with `uvotsource` using a circular aperture of radius $5''$, applying standard instrumental corrections and calibrations (T. S. Poole et al. 2008). For broadband spectral fitting with SPEX, filter count rates and the corresponding response matrices were generated for each filter.

3. SPECTRAL ENERGY DISTRIBUTION

In this section we present our modelling of the SED of Mrk 335, considering both the individual epochs and the time-averaged SED. To derive the intrinsic AGN continuum from the optical/UV to the X-ray band, we simultaneously account for the host-galaxy starlight, UV/optical reddening, and line-of-sight X-ray absorption toward the nucleus. The physical components included in the fits (accretion disc, Comptonisation, reflection, and host-galaxy contributions) are summarised in Table 2 together with their best-fit parameter values. The cosmological redshift (`reds`) was fixed at $z = 0.0258$ (C. J. Grier et al. 2012), corresponding to a luminosity distance of $D_L = 112.7 \text{ Mpc}$ (for $H_0 = 70 \text{ km s}^{-1} \text{ Mpc}^{-1}$, $\Omega_\Lambda = 0.70$, and $\Omega_m = 0.30$). The abundances of all absorption components were set to the protosolar values of K. Lodders et al. (2009). The resulting average intrinsic SED is shown in Fig. 3, while the bottom panel displays the best-fit SED for each epoch in June 2021. Below we describe the individual components adopted in the SED modelling.

3.1. Primary optical-UV-X-ray emission of the AGN

We modelled the observed primary hard X-ray continuum with a power-law component (`pow`), which mimics the Compton up-scattering of disc photons in an optically thin, hot corona (D. R. Wilkins & L. C. Gallo 2015; L. Keek

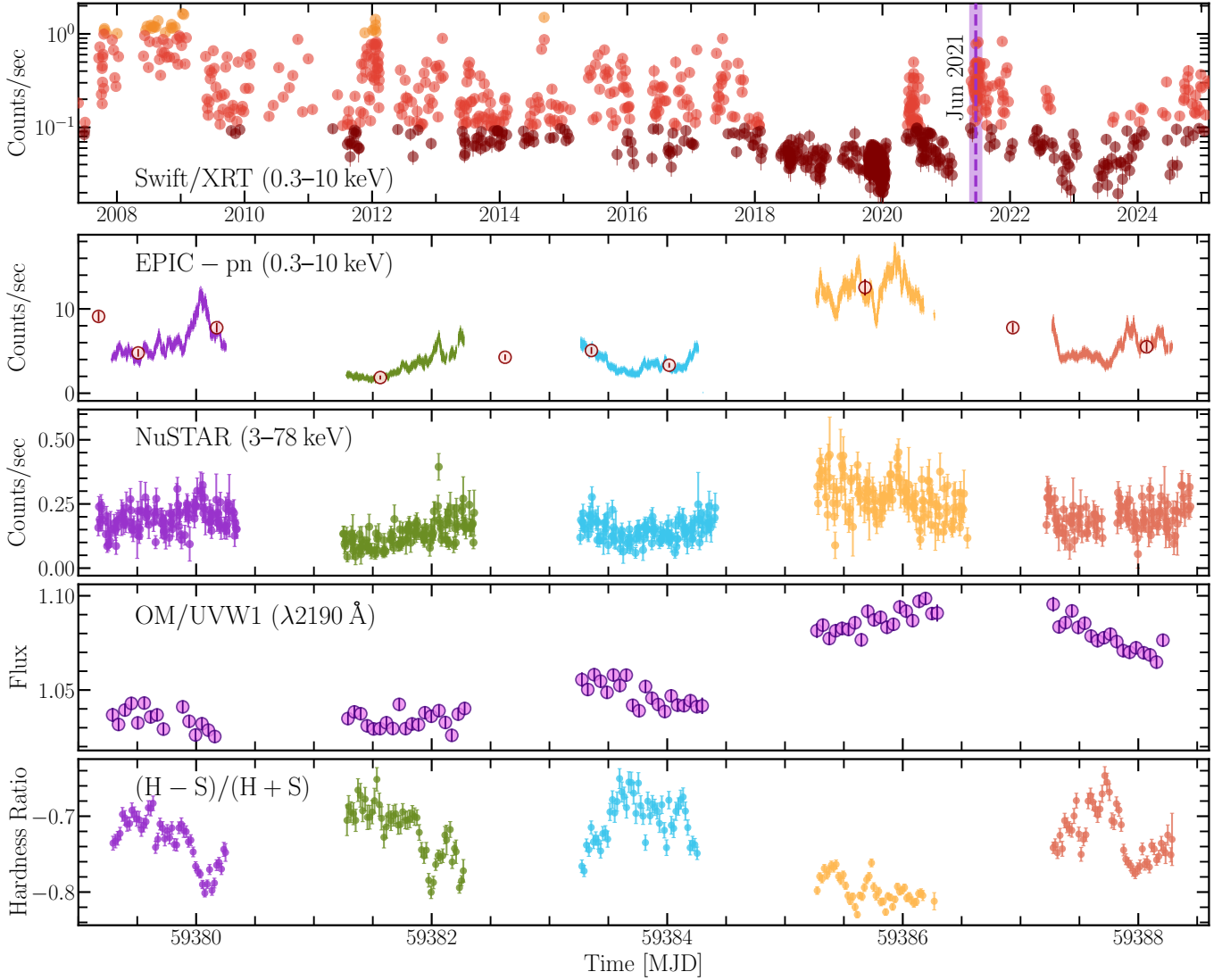


Figure 2. Multiwavelength light curves of Mrk 335. *Top panel:* Long-term *Swift*/XRT monitoring up to May 2025. The vertical dashed line marks the epoch of the joint *XMM-Newton* and *NuSTAR* campaign. We indicate the approximate high-, mid- and low- flux states with the color palette yellow, red and brown. *Second panel:* *XMM-Newton*/EPIC-pn light curves in the 0.3–10 keV band for the five observed epochs. The *Swift*/XRT points are overplotted after rescaling with *WebPIMMS*^a to match the EPIC-pn count rate. *Third panel:* *NuSTAR* FPMA light curve in the 3–78 keV band. *Fourth panel:* Optical/UV light curve from the OM UVW1 filter, shown in units of 10^{-14} erg cm $^{-2}$ s $^{-1}$ Å $^{-1}$. *Bottom panel:* Hardness ratio defined as $HR = (H - S)/(H + S)$, where S and H are the *XMM-Newton*/EPIC-pn count rates in the 0.3–2 keV and 2–10 keV bands, respectively.

^a<https://heasarc.gsfc.nasa.gov/cgi-bin/Tools/w3pimms/w3pimms.pl>

& D. R. Ballantyne 2016). Based on the analysis of the *NuSTAR* observations, a high-energy exponential cut-off was applied at 150 keV, consistent with the value reported by L. Keek & D. R. Ballantyne (2016). In addition, a low-energy cut-off was imposed to avoid exceeding the energy of the seed disc photons, by coupling the turnover energy to the temperature of the disc blackbody component. The photon index Γ varies across the observations, ranging from 1.94 to 2.08.

In addition to the primary power-law continuum, the spectrum below 2 keV exhibits a clear “soft excess” (K. A. Pounds et al. 1987; P. M. O’Neill et al. 2007). Its physical origin remains debated and is often attributed to warm Comptonisation of disc photons in a “warm corona” (see also P. Magdziarz & A. A. Zdziarski 1995; C. Done et al. 2012; P. O. Petrucci et al. 2018) and/or relativistically blurred ionised reflection from the accretion disc (e.g. J. Crummy

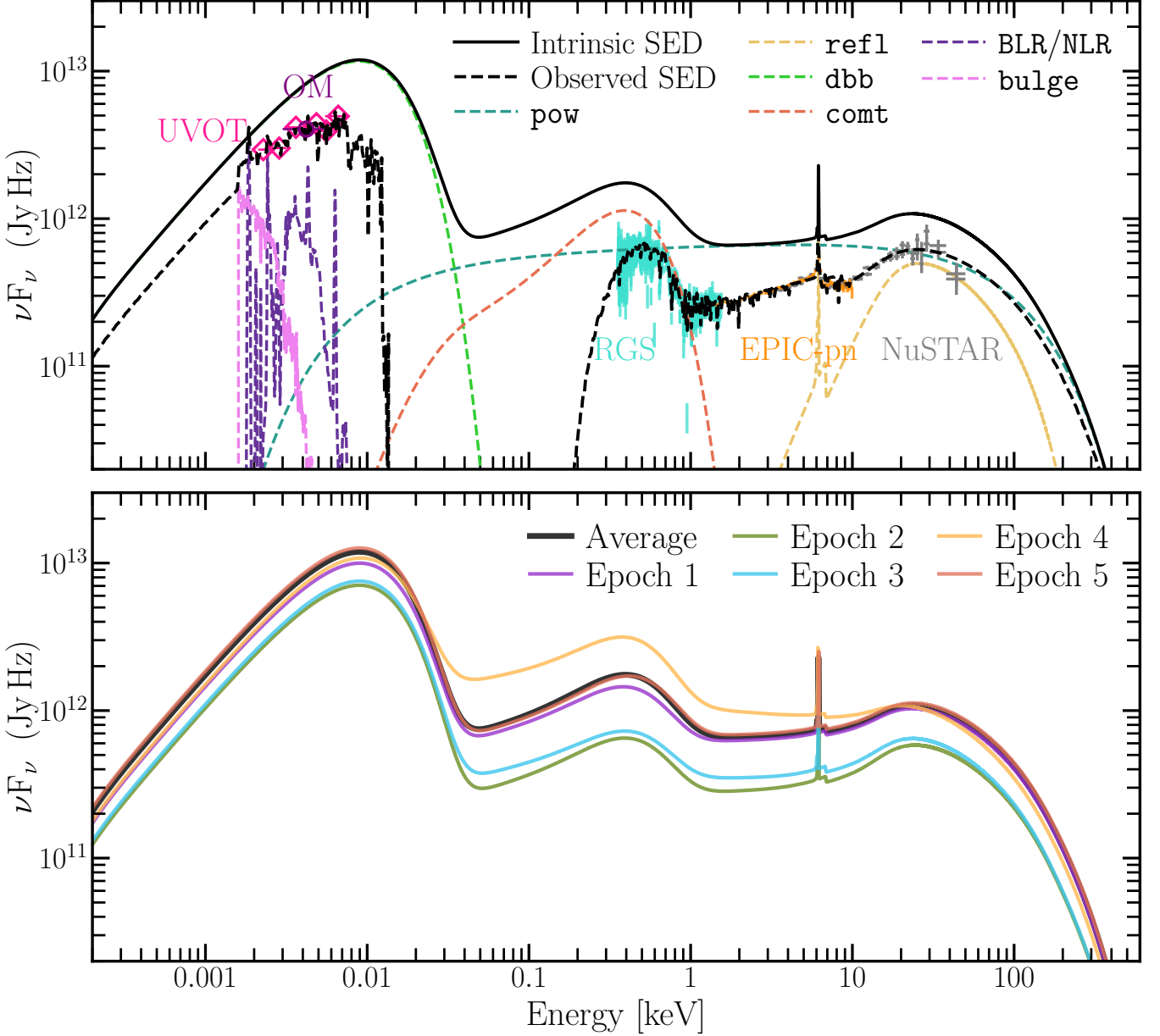


Figure 3. Spectral energy distribution (SED) modelling of Mrk 335. *Top:* Time-averaged SED modeling with the best-fit model components overplotted (see text for a description of each component), together with the multiwavelength data used in the modelling: XMM/EPIC-pn (orange), NuSTAR (gray), *Swift*/UVOT (magenta), XMM/OM (purple), and XMM/RGS (cyan). The intrinsic SED (all absorption removed) is shown as a solid black line, while the absorbed (observed) SED is shown as a dashed black line. For visual clarity, the model curves are displayed at an arbitrary energy resolution. *Bottom:* Best-fit SED models for the individual XMM/NuSTAR epochs in June 2021.

et al. 2006; J. García et al. 2013). Here we model this feature with a phenomenological Comptonisation component (`comt` in SPEX; L. Titarchuk 1994), without attempting to distinguish between physical scenarios. This approach has been successfully applied in similar contexts (e.g. NGC 3227; M. Mehdipour et al. 2021) and is sufficient to capture the ionising continuum required for our photoionisation modelling of the outflows, while being computationally more efficient.

The free parameters of `comt` are its normalisation, the seed-photon temperature (T_{seed}), the electron temperature (T_e), and the optical depth (τ) of the scattering plasma. In our modelling, T_{seed} was tied to the maximum temperature of the accretion disc (T_{max}) described by the `dbb` model, which assumes a geometrically thin, optically thick Shakura–

Table 2. Best-fit parameters of the SED model (dbb+comt+pow+refl)*3pion*ebv*reds*2hot.

Parameter	Average	Epoch 1	Epoch 2	Epoch 3	Epoch 4	Epoch 5
Power-law (pow)						
Norm. ^a	6.18 ± 0.03	5.86 ± 0.06	2.63 ± 0.07	3.31 ± 0.08	10.10 ± 0.07	6.40 ± 0.09
Γ	1.95 ± 0.01	1.96 ± 0.01	1.94 ± 0.02	1.98 ± 0.02	2.08 ± 0.01	1.95 ± 0.01
Warm Comptonization (comt)						
Norm. ^a	12.7 ± 0.2	10.5 ± 0.5	4.6 ± 0.3	4.5 ± 0.3	23.6 ± 0.7	11.0 ± 0.05
kT_e^c	0.118 ± 0.001	0.115 ± 0.002	0.117 ± 0.003	0.117 ± 0.003	0.117 ± 0.001	0.123 ± 0.001
τ	50^f	50^f	50^f	50^f	50^f	50^f
Disc blackbody (dbb)						
Norm. ^b	2.60 ± 0.03	2.17 ± 0.3	1.55 ± 0.02	1.64 ± 0.2	2.24 ± 0.04	2.76 ± 0.03
kT^c	7.56 ± 0.09	7.56^f	7.56^f	7.56^f	7.56^f	7.56^f
Cold reflection (refl)						
Scale, s	0.88 ± 0.3	0.89 ± 0.07	1.3 ± 0.1	1.3 ± 0.1	0.75 ± 0.06	0.86 ± 0.08
Galactic absorption (hot, ebv)						
$N_{\text{H,cold}}^d$	3.3^f	3.3^f	3.3^f	3.3^f	3.3^f	3.3^f
kT_{cold}^c	0.001^f	0.001^f	0.001^f	0.001^f	0.001^f	0.001^f
$N_{\text{H,warm}}^d$	$0.30^{+0.17}_{-0.13}$	0.30^f	0.30^f	0.30^f	0.30^f	0.30^f
kT_{warm}^c	61^{+12}_{-10}	61^f	61^f	61^f	61^f	61^f
$E(B - V)$	0.03^f	0.03^f	0.03^f	0.03^f	0.03^f	0.03^f
Fluxes^e						
$F_{0.3-10 \text{ keV}}$	13.2 ± 0.1	13.6 ± 0.1	7.15 ± 0.2	8.23 ± 0.2	25.5 ± 0.2	12.3 ± 0.2
$L_{0.3-10 \text{ keV}}$	4.89 ± 0.02	4.68 ± 0.05	2.16 ± 0.06	2.52 ± 0.06	8.34 ± 0.06	5.53 ± 0.08
L_{ion}	15.4 ± 0.1	15.1 ± 0.5	8.0 ± 0.3	9.1 ± 0.4	23.9 ± 0.5	17.5 ± 0.1
C-stat/dof	2353/1180	1466/1173	1555/1170	1608/1171	1535/1173	1677/1174

NOTE—Fixed parameters in the spectral energy distribution analysis are indicated with (^f).

^a Units: $10^{51} \text{ ph s}^{-1} \text{ keV}^{-1}$ (pow), $10^{53} \text{ ph s}^{-1} \text{ keV}^{-1}$ (comt).

^b Units: 10^{28} cm^2 (dbb).

^c Units: eV (kT_{seed} , kT_{dbb}), keV (kT_e).

^d Units: 10^{20} cm^{-2}

^e Observed flux in units of $10^{-12} \text{ erg cm}^{-2} \text{ s}^{-1}$. Intrinsic X-ray luminosity and ionising luminosity in units of $10^{43} \text{ erg s}^{-1}$

Sunyaev accretion disc (N. I. Shakura & R. A. Sunyaev 1973). This disc component accounts for the optical/UV emission of Mrk 335. Because the disc temperature is not expected to vary significantly on week-long timescales (see also the OM light curve in Fig. 2), and given its strong degeneracy with the dbb normalisation due to nearby continuum absorption by neutral hydrogen, we determined T_{dbb} from the average spectrum and restricted it in the single-epoch fits to lie within the uncertainty of that measurement. We found a best-fit temperature of $kT_{\text{dbb}} = 7.56 \pm 0.09 \text{ eV}$.

3.2. Reflected X-ray continuum

The EPIC-pn and NuSTAR spectra of Mrk 335 show clear evidence of X-ray reflection, most prominently the Fe K α emission line at $\sim 6.4 \text{ keV}$ and the high-energy Compton hump above 10 keV . To account for this, we included a cold reflection component (refl in SPEX; P. Magdziarz & A. A. Zdziarski 1995; P. T. Zycki & B. Czerny 1994) that reprocesses the primary X-ray continuum. In our implementation, the reflection spectrum is tied to the same photon index and high-energy cut-off as the observed power-law continuum, while the ionisation parameter was fixed to zero to approximate reflection from neutral material with solar abundances.

The main free parameter is the reflection scaling factor, which varies modestly (0.75–1.5) between epochs. This level of variability is plausible, although assuming that the incident continuum is identical to the observed one is

a simplification. We note that `refl` provides a simplified description and does not include relativistic effects from the innermost accretion disc, nor a possible broadened Fe K α component. A more sophisticated reflection model would be required to capture those features. The model also does not include any contribution from lighter ions (e.g. oxygen, nitrogen) and Fe-L which might also contribute to the soft excess. For the purposes of the present SED modelling, however, this simplistic approach is sufficient to reproduce the overall shape of the broadband emission (e.g. D. Rogantini et al. 2022a).

3.3. Galactic absorption and reddening

In modelling the X-ray spectra of Mrk 335, we accounted for absorption by the cold, neutral ISM in the Galaxy. This was implemented with the `hot` component in `SPEX`, which computes the transmitted spectrum of a plasma in collisional ionisation equilibrium. To approximate neutral absorption, we fixed the plasma temperature to $kT = 1 \times 10^{-6}$ keV ($T \simeq 10$ K), and adopted a hydrogen column density of $N_{\text{H}} = 3.30 \times 10^{20}$ cm $^{-2}$ (HI4PI Collaboration et al. 2016).

For the optical/UV data from *Swift*/UVOT and XMM-*Newton*/OM (UVW1 filter only), we corrected for Galactic dust reddening using the multiplicative `ebv` component in `SPEX`. This model applies the extinction curve of J. A. Cardelli et al. (1989), with the near-UV update by J. E. O’Donnell (1994). Based on the recalibration by E. F. Schlafly & D. P. Finkbeiner (2011), we adopted $E(B - V) = 0.030$ mag and fixed the total-to-selective extinction ratio to the Galactic average, $R_V = 3.1$.

We also tested for the presence of a warmer Galactic ISM phase by adding a second `hot` component with temperature left free. The deep RGS spectra (Section 4.1) indeed constrain a warmer phase with $kT = 61$ eV, which we keep fixed, together with its column density, in the single-epoch SED fits. Finally, we investigated whether intrinsic cold absorption and reddening in Mrk 335 could contribute by adding an additional `hot` and `ebv` component at the systemic redshift of the source. These components did not improve the fit, indicating that any intrinsic neutral absorption is negligible.

In contrast, the spectra clearly require multiple layers of ionised absorption. Three photoionisation components are necessary to model the ionised outflows in Mrk 335. These outflows are the main focus of this work and their modeling is described in Section 4 and summarised in Table 3.

3.4. Emission from the BLR/NLR and galactic bulge

The optical/UV photometric bands of *Swift*/UVOT and XMM-*Newton*/OM include not only the AGN continuum, but also emission from the broad-line region (BLR) and narrow-line region (NLR). To account for this contribution in the SED modeling, we adopted the empirical emission model of M. Mehdipour et al. (2015), originally developed for NGC 5548, as a template. This model accounts for the Balmer continuum, the Fe II pseudo-continuum, and strong emission lines from the BLR and NLR. For simplicity, we assumed the BLR/NLR emission to be constant across the five XMM-*Newton* epochs. The predicted H β flux from our approximate modelling is $\sim 2 \times 10^{-13}$ erg cm $^{-2}$ s $^{-1}$, lower than the fluxes reported by C. J. Grier et al. (2012) during the 2010 campaign, where $F(\text{H}\beta)$ varied between $(5-6) \times 10^{-13}$ erg cm $^{-2}$ s $^{-1}$.

The circular extraction apertures of *Swift*/UVOT (radius 5'') inevitably include starlight from the host galaxy of Mrk 335. To correct for this contribution, we adopted the optical bulge flux derived by M. C. Bentz et al. (2013) from HST imaging. They modelled the stellar emission from the galaxy bulge using a rectangular aperture of $5'' \times 7.6''$, comparable in size to the UVOT aperture. From their modelling of images taken with the F550M medium-band V filter (exposure of 2040 s), we recalculated the expected flux for our UVOT aperture, obtaining a bulge flux of 1.16×10^{-15} erg cm $^{-2}$ s $^{-1}$ Å $^{-1}$ at 5231 Å with an estimated uncertainty of $\sim 10\%$.

To extend this estimate across the optical/UV range, we adopted the galaxy bulge spectral template of A. L. Kinney et al. (1996), widely used in previous AGN SED studies (e.g. M. Mehdipour et al. 2015, 2018). We scaled the template to match the measured bulge flux at 5231 Å and used it to estimate the stellar-bulge contribution at the wavelengths covered by the OM and UVOT filters. In the top panel of Fig. 3, the contributions of the host bulge and the BLR/NLR emission are shown as dashed pink and purple curves, respectively.

4. MODELING OF THE IONISED OUTFLOW

Modeling high-resolution RGS spectra, we find that, in line with past observations, the complex ionised outflow system remains present in the intermediate flux state. The photoionisation modelling of the winds for the stacked spectrum and for the individual epochs is described in the following subsections.

Table 3. Best-fit parameters of the ionised outflow components obtained with the `pion` model.

Parameter	Average	Epoch 1	Epoch 2	Epoch 3	Epoch 4	Epoch 5
High-ξ wind						
N_{H}^{a}	13_{-4}^{+8}	25_{-15}^{+38}	$3.4_{-2.3}^{+4.4}$	40_{-25}^{+50}	13_{-7}^{+14}	$3.5_{-1.7}^{+3.3}$
$\log \xi^{\text{b}}$	$3.63_{-0.08}^{+0.09}$	3.6 ± 0.1	$3.3_{-0.2}^{+0.1}$	$3.51_{-0.06}^{+0.09}$	$3.67_{-0.06}^{+0.07}$	3.66 ± 0.07
f_{cov}	1^f	1^f	1^f	1^f	1^f	1^f
$v_{\text{turb}}^{\text{c}}$	90 ± 20	110 ± 30	90^f	90^f	80 ± 30	125_{-40}^{+60}
$v_{\text{out}}^{\text{c}}$	-5820_{-40}^{+60}	-5800_{-150}^{+160}	-5800_{-120}^{+140}	-5900 ± 110	-5670_{-170}^{+110}	-6410_{-140}^{+150}
Mid-ξ wind						
N_{H}^{a}	$2.0_{-0.5}^{+0.6}$	$3.5_{-0.9}^{+1.2}$	$7.4_{-3.3}^{+10.3}$	$1.1_{-0.4}^{+0.6}$	$2.0_{-0.3}^{+0.4}$	$1.2_{-0.4}^{+0.5}$
$\log \xi^{\text{b}}$	3.10 ± 0.05	$3.08_{-0.06}^{+0.05}$	$3.45_{-0.06}^{+0.61}$	$2.92_{-0.12}^{+0.11}$	2.99 ± 0.04	3.03 ± 0.12
f_{cov}	0.57 ± 0.05	0.57^f	0.57^f	0.57^f	0.57^f	0.57^f
$v_{\text{turb}}^{\text{c}}$	780_{-80}^{+100}	790_{-120}^{+160}	780^f	780^f	810_{-100}^{+130}	900_{-140}^{+170}
$v_{\text{out}}^{\text{c}}$	-3210_{-110}^{+90}	-2700_{-200}^{+190}	-3190_{-310}^{+280}	-3380_{-340}^{+290}	-2990_{-140}^{+120}	-3600_{-220}^{+220}
Low-ξ wind						
N_{H}^{a}	0.18 ± 0.05	$0.26_{-0.08}^{+0.13}$	$0.68_{-0.13}^{+0.12}$	$1.2_{-0.2}^{+0.3}$	0.09 ± 0.02	$0.69_{-0.11}^{+0.14}$
$\log \xi^{\text{b}}$	2.01 ± 0.03	$2.11_{-0.07}^{+0.06}$	2.03 ± 0.04	$2.04_{-0.07}^{+0.05}$	$1.88_{-0.08}^{+0.06}$	2.13 ± 0.04
f_{cov}	$0.67_{-0.09}^{+0.15}$	0.67^f	0.67^f	0.67^f	0.67^f	0.67^f
$v_{\text{turb}}^{\text{c}}$	280_{-70}^{+120}	180_{-70}^{+90}	280^f	280^f	170_{-40}^{+50}	90_{-30}^{+40}
$v_{\text{out}}^{\text{c}}$	-2140 ± 70	-2440_{-140}^{+150}	-2020_{-100}^{+110}	-2230_{-160}^{+140}	-2090 ± 100	-2520_{-70}^{+120}
C-stat/dof	1783/1462	1642/1435	1740/1442	1676/1443	1579/1434	1760/1437

NOTE—Average values represent the best-fit parameters from the stacked RGS spectrum. Fixed parameters are indicated with (f). For single-epoch fits, f_{cov} was fixed to the stacked-spectrum value (and for the high- ξ component fixed to unity).

^a Units: 10^{22} cm^{-2} .

^b Ionisation parameter, ξ , in erg cm s^{-1} .

^c Velocities in km s^{-1} .

4.1. The deep RGS spectrum

To characterise the numerous absorption features produced by the ionised outflows in Mrk 335, we employed the `pion` model in `SPEX` (J. M. Miller et al. 2015; M. Mehdipour et al. 2016). This self-consistent photoionisation model simultaneously computes the ionisation and thermal balance of the plasma, together with its resulting spectrum, under the assumption of photoionisation equilibrium (PIE). The calculation is based on the SED derived in Section 3 from the continuum components of our model using the stacked XMM-*Newton*, NuSTAR and *Swift* data.

We first obtained the best-fit model for the stacked 2021 RGS spectrum of Mrk 335 (net exposure of 440 ks), and then used this model as the baseline for fitting the individual RGS spectra. Figure 4 shows the stacked spectrum in the source rest frame, with the main absorption lines indicated. To reproduce the absorption features from the different ionic species, three distinct `pion` components with different ionisation parameters ξ are required (C. B. Tarter et al. 1969). The ionisation parameter is defined as $\xi = L_{\text{ion}}/(n_{\text{H}}r^2)$, where L_{ion} is the ionising luminosity in the 1–1000 Ry band (13.6 eV to 13.6 keV) in erg s^{-1} , n_{H} is the hydrogen density in cm^{-3} , and r is the distance between the ionising source and the photoionised plasma in cm. Starting from the continuum model, adding one `pion` component improves the fit by $\Delta C = 990$ for five additional free parameters. Adding a second and third `pion` component yields further improvements of $\Delta C = 400$ (five free parameters) and $\Delta C = 90$ (four free parameters, with f_{cov} fixed to unity), respectively. The best-fit parameters of the three components are reported in Table 3. We explored column densities down to 10^{19} cm^{-2} , ionisation parameters in the range $\log \xi = -1$ to 5.5, and outflow velocities from a few hundred

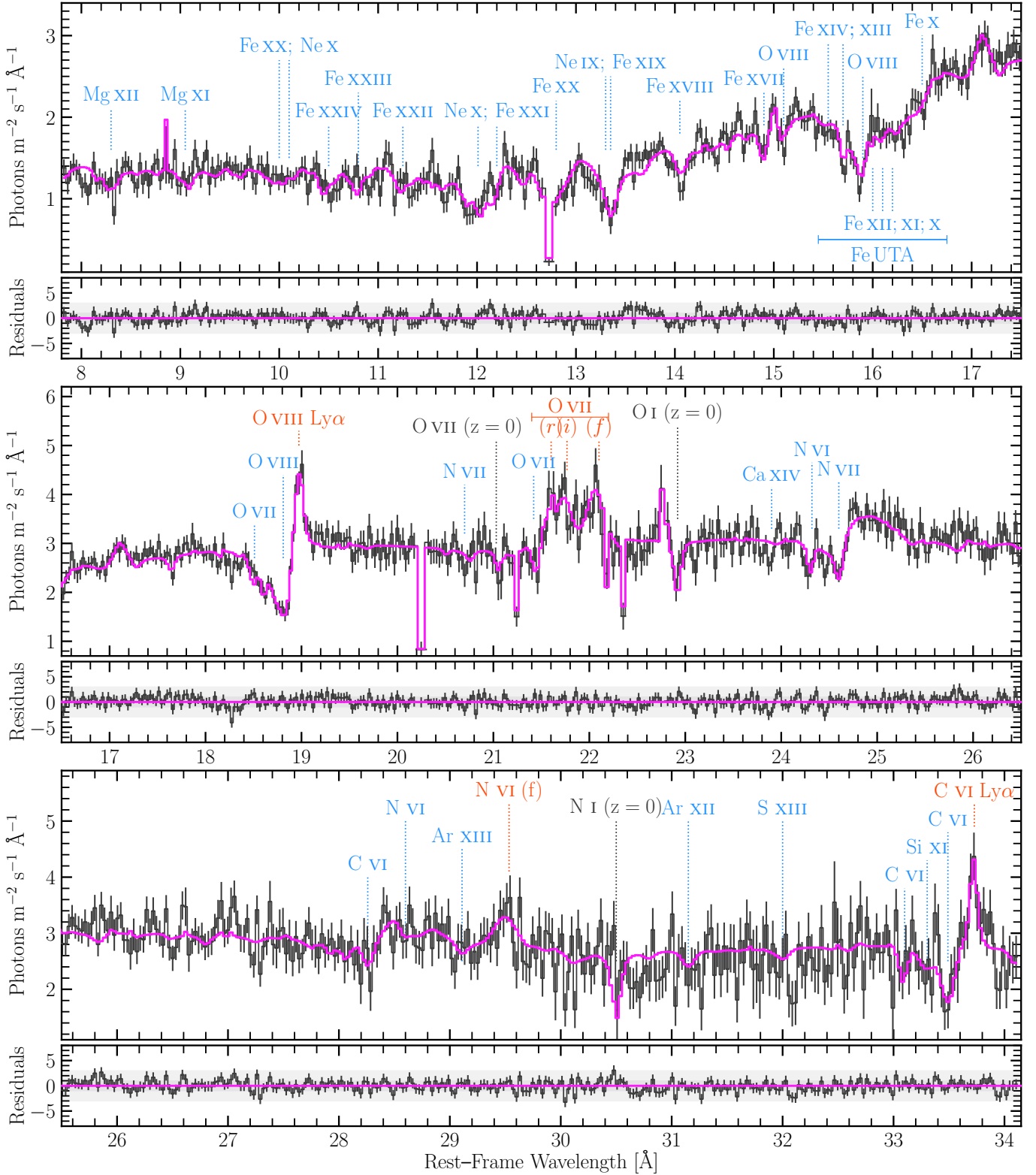


Figure 4. Segments of the stacked RGS spectrum of Mrk 335 (net exposure of 440 ks), shown in the rest frame of the source. The magenta line represents the best-fit photoionisation model. Prominent absorption and emission features are marked with blue and red labels, respectively, while Galactic absorption lines at $z = 0$ are indicated in black. The absorption features are systematically blueshifted, tracing ionised outflows. Narrow and broad emission lines (e.g. O VII, O VIII, C VI) are also detected. For display purposes, the RGS1 and RGS2 spectra have been combined in this figure; they were fitted simultaneously in the analysis.

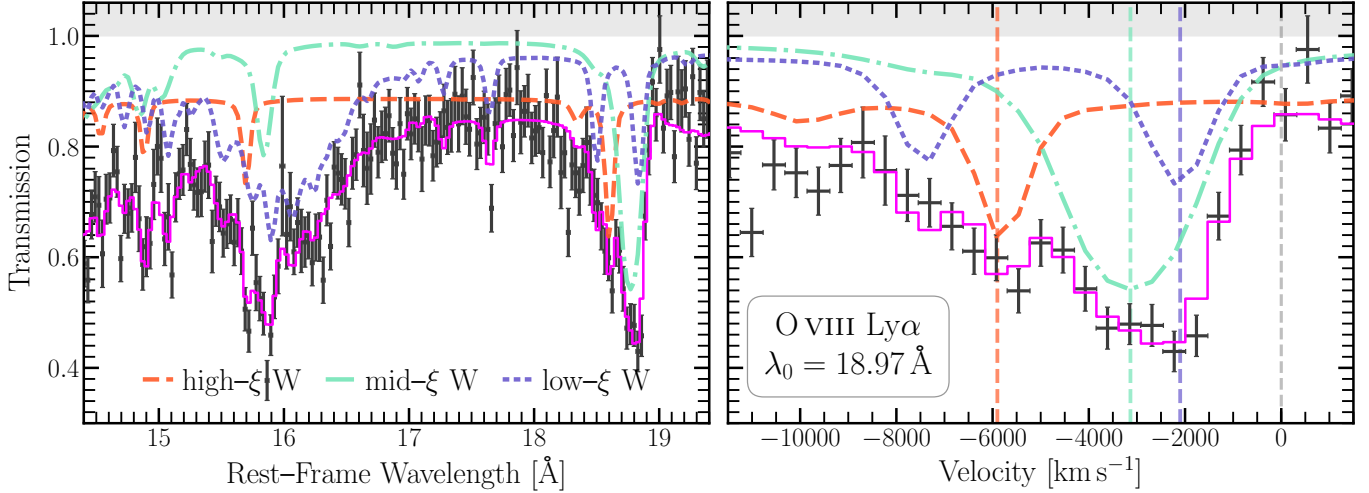


Figure 5. *Left panel:* Transmission spectrum of Mrk 335, obtained by dividing the observed RGS spectrum by the intrinsic continuum model. The plot zooms in on two key regions: the Fe UTA (15.5–16.5 Å) and the O VIII Ly α line (~ 18.7 Å). The low- ξ wind component provides the dominant contribution to the Fe UTA, while all three ionisation components are required, in different proportions, to reproduce the O VIII absorption profile. *Right panel:* Zoom-in on the O VIII Ly α absorption line, shown in velocity space with respect to the rest-frame wavelength of 18.97 Å. The black data points and magenta line represent the transmitted RGS spectrum and best-fit model, respectively, while the coloured curves show the transmission of the individual photoionised wind components. The low-, mid-, and high- ξ winds are shown in blue, green, and orange, respectively. Vertical dashed lines mark the best-fit outflow velocities: $v_{\text{out}} = -2100$ km s $^{-1}$ (low- ξ), $v_{\text{out}} = -3135$ km s $^{-1}$ (mid- ξ), and $v_{\text{out}} = -5900$ km s $^{-1}$ (high- ξ). The figure highlights that the O VIII absorption is shaped by the superposition of all three wind components, each contributing with different velocities and strengths.

km s $^{-1}$ up to mildly relativistic values; however, adding a fourth component is not statistically required ($\Delta C < 10$ for four additional free parameters).

The low-ionisation component (low- ξ wind) accounts for absorption from M-shell Fe ions, producing the broad unresolved transition array (UTA) at ~ 16 – 17 Å (E. Behar et al. 2001). It also contributes to transitions from Be-like and Li-like ions such as Si XI, Mg IX, and Mg X, as well as the He-like Ne IX. The intermediate-ionisation component (mid- ξ wind) predominantly produces the He-like Ne IX and Mg XI lines, and dominates the H-like transitions of O VIII and Ne X, together with lines from Fe XVII–Fe XX. Finally, the high-ionisation component (high- ξ wind) is required to reproduce the strongest H-like O VIII and Ne X absorption, and contributes significantly to highly ionised iron species such as Fe XXI, Fe XXII, and Fe XXIII within the RGS band. Models with fewer components fail to reproduce the full set of detected transitions in the deep, line-rich RGS spectrum.

The absorption lines are systematically blueshifted with respect to their rest-frame wavelengths, indicating that the ionised gas is outflowing. We identify three distinct velocity components at ~ -2100 , ~ -3200 , and ~ -5900 km s $^{-1}$, corresponding to the low-, mid-, and high- ξ wind components, respectively. Figure 5 (left panel) shows how the low- ξ wind accounts for the UTA feature, and demonstrates that the full three-component ionisation/velocity structure is required to reproduce the observed O VIII line profile. The right panel shows the velocity profile of the O VIII Ly α absorption line, where the contributions of the three components are evident. Approximately 12%, 57%, and 31% of the total O VIII Ly α equivalent width arise from the high- ξ , mid- ξ , and low- ξ winds, respectively.

In the time-averaged spectrum, we allowed the column density N_{H} and covering fraction f_{cov} to vary for all three wind components. All three components require substantial columns, with $N_{\text{H}} \sim 10^{21}$ – 10^{23} cm $^{-2}$ from the low- to the high-ionisation phases. For the high- ξ component, f_{cov} is strongly degenerate with N_{H} because its transmission is close to featureless and is constrained mainly by narrow, high-ionisation absorption lines. This degeneracy can be reduced when the transmission shows appreciable curvature, since curvature driven by the total absorbing column differs from that produced by partial covering. We therefore fixed the high- ξ covering fraction to unity in the stacked-spectrum fit. Figure 6 shows the model transmission spectra of the three pion components (solid black lines) for the stacked spectrum, illustrating their respective contributions to the total absorption. The low- ξ component produces most of the broad absorption in the Fe UTA region, while the high- ξ component contributes primarily to the strongest

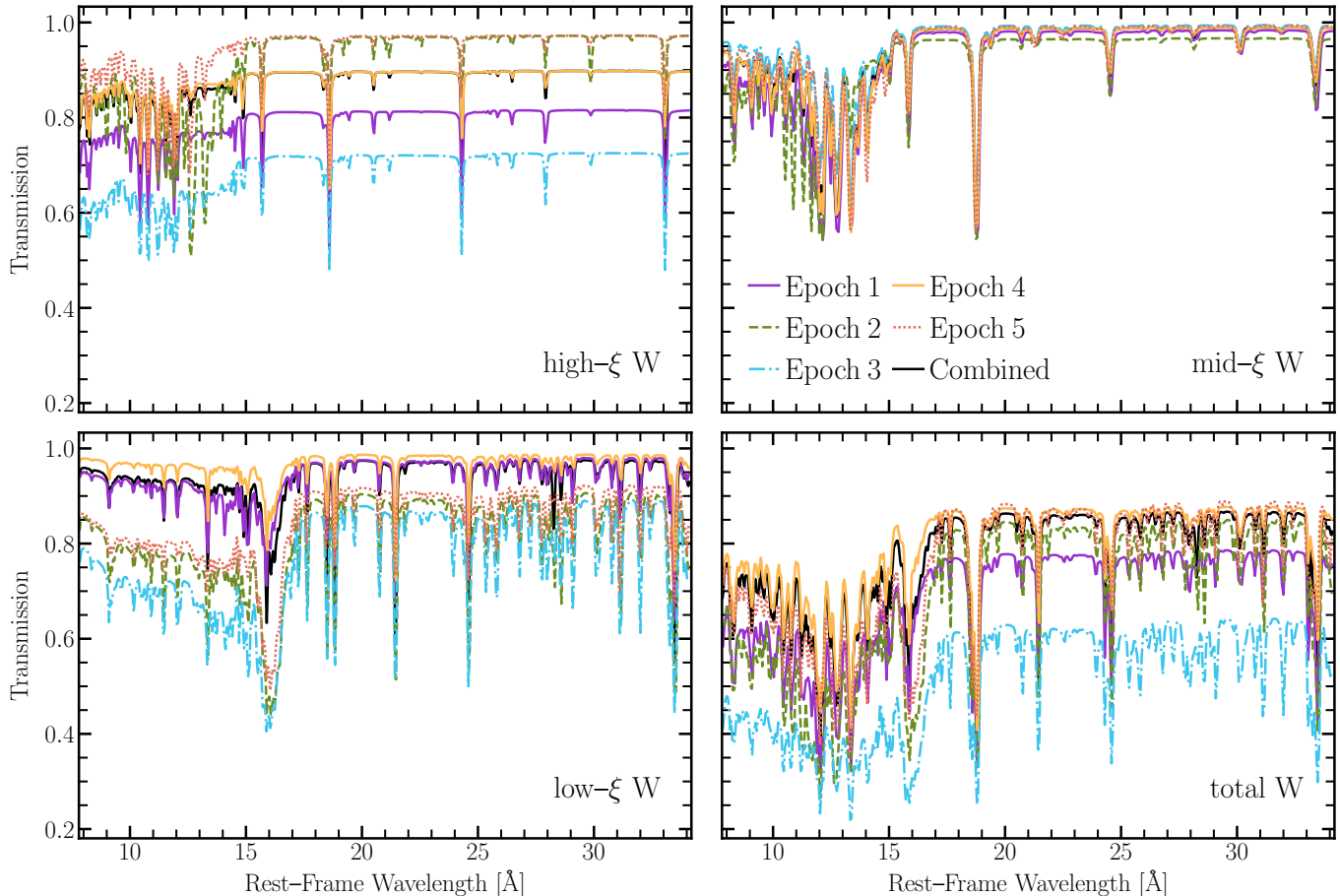


Figure 6. Evolution of the model transmission spectra of the photoionised wind in Mrk 335. From top to bottom, the panels show the high-, mid-, and low-ionisation components, and the total transmission (product of all components), for the five XMM-Newton epochs (color-coded). Changes in both the depth and detailed line structure, most prominently in the Fe XVII–O VIII band, trace variations in the physical state of the outflow. The low-ionisation component dominates the Fe UTA region, while the high-ionisation component contributes most strongly to the O VIII absorption.

high-ionisation lines (in particular O VIII). The mid- ξ phase contributes to both regimes and shapes the intermediate-ionisation line forest.

We also modelled the turbulent velocities v_{turb} , which determine the line broadening. The derived values are ~ 90 – 280 km s^{-1} for the low- and high- ξ winds, and significantly larger for the mid- ξ wind, reaching $\sim 780 \text{ km s}^{-1}$.

In addition to the absorption features, the RGS spectrum of Mrk 335 shows narrow and broad emission lines. To avoid overloading the fit computation, we modelled these lines phenomenologically with Gaussian profiles. The line identification, centroid energy, normalisation, and width are reported in Table 4. Both the O VIII and C VI Ly α lines require a narrow and a broad component; the narrow and broad components have FWHM of approximately 0.2 \AA and 4 \AA , respectively. The O VII triplet is detected through its resonance, intercombination, and forbidden lines. Physical modeling of the emission lines (e.g. M. L. Parker et al. 2019) will be performed in follow-up studies; here they are included simply to ensure high fidelity constraints on the parameters of the ionized absorption models.

4.2. The variability of the wind components

To investigate the variability of the three photoionised wind components, we fitted each RGS epoch independently, using the best-fit model of the stacked RGS spectrum as the initial guess. The covering fractions of the three absorbers were fixed to the average values obtained from the stacked spectrum. Given the limited signal-to-noise ratio of the single-epoch spectra, the degeneracy between column density and covering fraction cannot be broken. We also fixed the turbulent velocities in Epochs 2 and 3 to the average values from the stacked fit, since they could not be constrained

Table 4. X-ray emission lines detected in the stacked RGS spectrum of Mrk 335.

Line ID	Wavelength (Å)	Reference wavelength (Å)	Norm (10^{49} ph s $^{-1}$)	FWHM (Å)
C VI (broad)	$34.641^{+4.940}_{-0.817}$	33.738	$88.12^{+41.88}_{-25.74}$	$4.675^{+6.559}_{-1.623}$
C VI Ly α	33.724 ± 0.017	33.738	4.91 ± 0.93	< 0.161
N VI (<i>f</i>)	29.496 ± 0.035	29.552	3.74 ± 0.96	$0.215^{+0.060}_{-0.046}$
N VI (<i>i</i>)	28.870 ± 0.060	29.080	2.08 ± 0.83	0.215^c
N VI (<i>r</i>)	28.517 ± 0.050	28.781	3.12 ± 0.85	0.215^c
N VII Ly α	24.890 ± 0.038	24.791	6.83 ± 0.88	0.505 ± 0.086
O VII (<i>f</i>)	22.062 ± 0.021	22.105	6.29 ± 0.91	$0.182^{+0.025}_{-0.021}$
O VII (<i>i</i>)	21.741 ± 0.021	21.799	5.62 ± 0.78	0.182^c
O VII (<i>r</i>)	21.487 ± 0.022	21.603	4.58 ± 0.73	0.182^c
O VIII (broad)	18.874 ± 0.160	18.965	23.94 ± 2.34	3.310 ± 0.331
O VIII Ly α	18.975 ± 0.005	18.965	3.58 ± 0.33	0.063 ± 0.015
Fe XVII	17.081 ± 0.018	17.055	2.31 ± 0.47	$0.154^{+0.071}_{-0.038}$
O VII RRC	16.679 ± 0.035	16.771	1.51 ± 0.45	0.210 ± 0.100

NOTE—Line widths are in Å. We tied (^c) the FWHM of the forbidden, intercombination, and resonance lines of the N VI and O VII triplets, since they cannot be separated reliably. Reference wavelengths are taken from N. Hell et al. (2025) and references therein. “RRC” denotes a radiative recombination continuum, i.e. an emission edge produced when free electrons recombine into a bound level; the quoted reference wavelength for O VII RRC corresponds to the recombination edge (ionisation threshold) and is taken from J. S. Kaastra et al. (2008).

reliably in these two observations, which have the lowest signal-to-noise due to their low observed flux. For each pion component, we fitted the column density N_{H} , ionisation parameter ξ , and outflow velocity v_{out} .

For the broadband continuum, we adopted the SED model determined for each observation in the previous step of the analysis (Section 3). The photon index Γ and normalisation of the power-law component, as well as the temperature and normalisation of the Comptonisation component, were allowed to vary within 2σ of their best-fit values from the SED modelling. This allows a consistent adjustment of the continuum within the RGS band while accounting for the detailed absorption. During the fits to the individual RGS spectra, the normalisations of the emission lines were allowed to vary within 2σ of the best-fit values from the stacked spectrum, while all other Gaussian parameters were kept fixed. This implicitly assumes that these parameters are constant across epochs and that any apparent changes are consistent with their statistical uncertainties.

Figure 6 illustrates how the transmission spectra of each component vary across the observations. The differences between epochs show that the absorber opacity does not change as a simple normalisation: both the depth and the detailed line structure vary, consistent with changes in N_{H} and ξ (and, to a lesser extent, in the velocity field). The best-fit parameters of the ionised outflow components for each RGS observation are listed in Table 3. Figure 7 shows the evolution of the column density, ionisation parameter, and outflow velocity as a function of time (left panels) and ionising luminosity (right panels). Zoomed-in RGS spectra for each epoch are shown in Appendix A (Fig. 10).

5. DISCUSSION

Our deep XMM-Newton campaign captured Mrk 335 in an intermediate-flux state, revealing three photoionised absorption components associated with an obscuring outflow. The five consecutive observations enable, for the first time, a detailed characterisation of the short-timescale (days) variability of a multi-phase obscurer. Previous studies of obscurers in Seyfert 1 galaxies typically focused either on a single long observation (e.g. F. Zaidouni et al. 2024), on widely separated epochs (e.g. J. Mao et al. 2022b), or on events so optically thick that the RGS spectrum was strongly suppressed (e.g. J. S. Kaastra et al. 2014; E. Kara et al. 2021). This dataset therefore provides a more complete view of the structure, variability, and origin of obscurers in AGN.

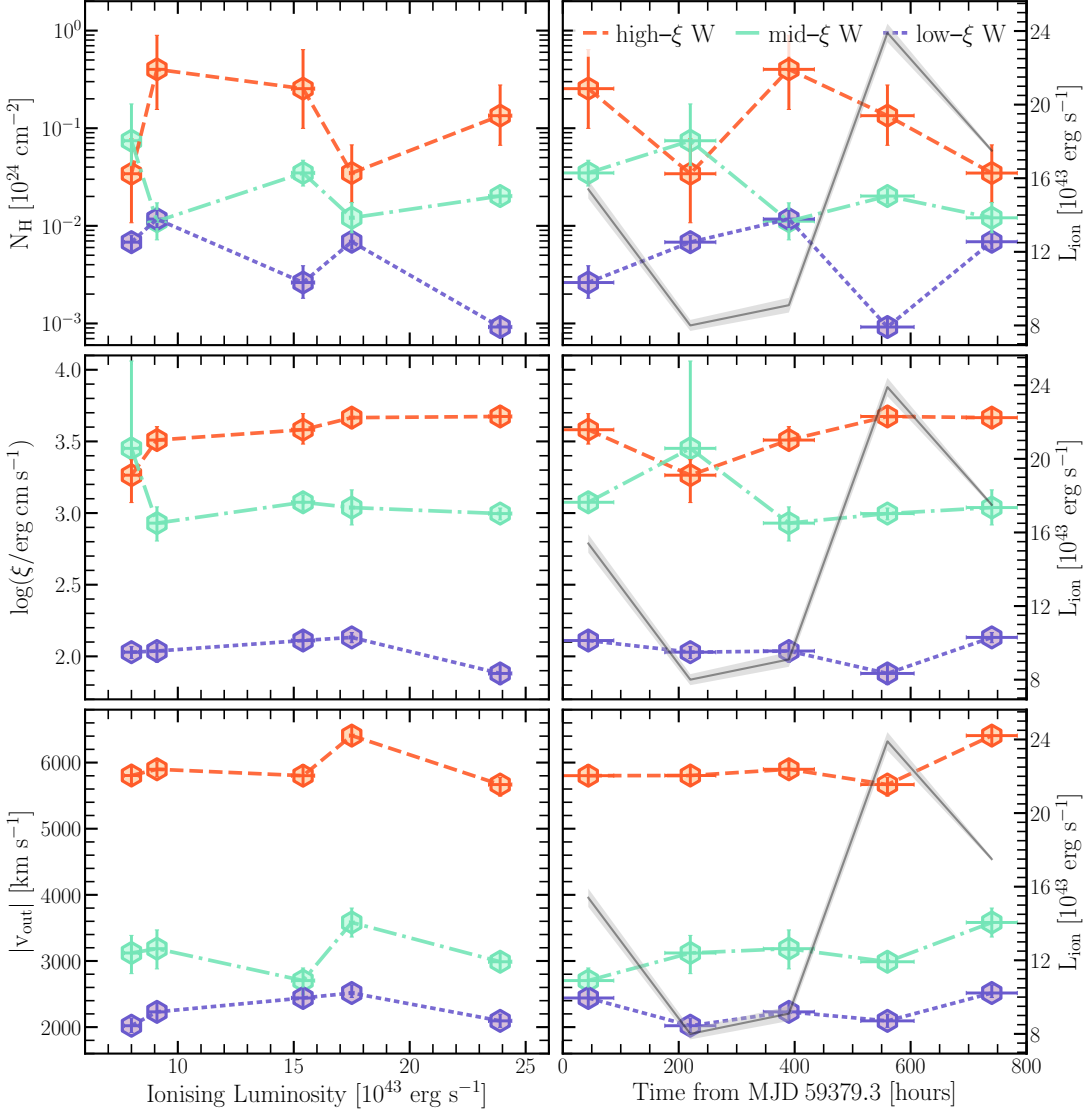


Figure 7. Evolution of the ionised outflow parameters of Mrk 335 across the 2021 campaign. *Left column:* wind parameters as a function of ionising luminosity L_{ion} (13.6 eV–13.6 keV). From top to bottom, the panels show the column density (N_{H}), the ionisation parameter ($\log \xi$), and the absolute outflow velocity ($|v_{\text{out}}|$). *Right column:* same parameters as a function of time since the start of the first observation. The shaded gray band indicates the temporal evolution of the ionising luminosity. Each point corresponds to one of the five XMM-Newton epochs, and the curves connect measurements of the same wind component. The orange, green, and blue series represent the high-, mid-, and low- ξ wind components, respectively.

5.1. Obscuring wind in Mrk 335

During the intermediate-flux phase, the RGS spectra of Mrk 335 reveal three distinct photoionised absorbers with time-averaged ionisation parameters of $\log \xi \simeq 3.63$ (high- ξ), 3.10 (mid- ξ), and 2.01 (low- ξ). The absorption lines are blueshifted by $v_{\text{out}} \approx 5800$ km s $^{-1}$, 3200 km s $^{-1}$, and 2150 km s $^{-1}$, respectively. These velocities are considerably higher than those typically found for classical warm absorbers (~ 100 –1000 km s $^{-1}$; A. J. Blustin et al. e.g. 2005; R. G. Detmers et al. e.g. 2011; S. Laha et al. e.g. 2014; E. Behar et al. e.g. 2017), and lower than the velocities attributed to ultra-fast outflows (UFOs), which can reach a substantial fraction of the speed of light (e.g. F. Tombesi et al. 2010; M. Audard et al. 2025). Instead, the velocities are comparable to the absorption troughs seen in the UV band during episodic obscuration events (e.g. J. S. Kaastra et al. 2014; F. Zaidouni et al. 2024). Although no simultaneous HST/COS spectra are available for our 2021 campaign, previous high-resolution UV observations have revealed broad absorption troughs with $v_{\text{out,UV}} \sim 4000$ –6500 km s $^{-1}$ (A. L. Longinotti et al. 2013, 2019; M. L. Parker

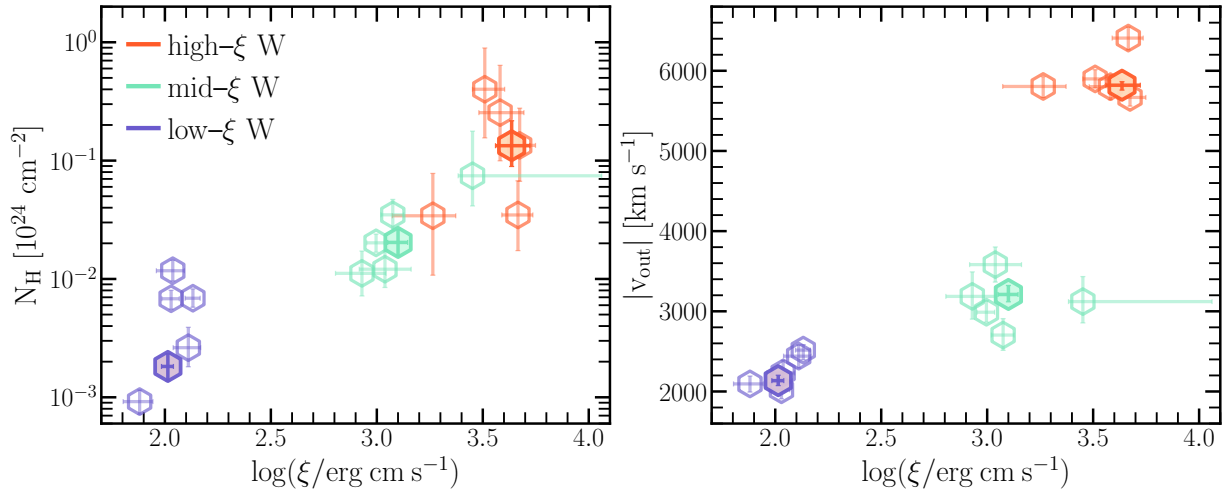


Figure 8. Outflow parameter correlations for Mrk 335. Left: column density N_{H} versus ionisation parameter $\log \xi$. Right: absolute outflow velocity $|v_{\text{out}}|$ versus $\log \xi$. Colours denote the three wind phases (high-, mid-, and low- ξ ; see legend). Open hexagons show the best-fit values for the individual epochs, while filled hexagons show the best-fit values for the stacked deep RGS spectrum.

et al. 2019). During the 2009 quasi-simultaneous XMM-Newton/HST observation, the velocity of the X-ray wind ($\sim 4000\text{--}6000 \text{ km s}^{-1}$) was similar to that of the UV absorption features ($\sim 6500 \text{ km s}^{-1}$), suggesting that the X-ray and UV absorbers are manifestations of the same obscuring structure (A. L. Longinotti et al. 2013). Interestingly, later HST/COS observations in July 2018 indicate that the UV absorber had slowed to $\sim 3000 \text{ km s}^{-1}$, closer to the velocities of the low- ξ and mid- ξ wind components observed in 2021 (M. L. Parker et al. 2019).

Figure 8 shows the location of the three wind components in the $(\log \xi, N_{\text{H}})$ and $(\log \xi, |v_{\text{out}}|)$ planes. The filled hexagons represent the best-fit parameters from the combined spectrum, while the open symbols show the values measured in the individual epochs (with their uncertainties). The three components occupy distinct regions of parameter space and, overall, the distribution is consistent with a stratified, multi-phase outflow, where both N_{H} and $|v_{\text{out}}|$ increase with ionisation (see the XRISM study of NGC 4151 for a similar phenomenology and discussion of wind stratification; X. Xiang et al. 2025). In this context, the left panel can be viewed as a discrete sampling of the absorption measure distribution (AMD; T. Holzer et al. 2007; E. Behar 2009), defined as $\text{AMD} \equiv dN_{\text{H}}/d \log \xi \propto \xi^m$. As discussed for NGC 4151, the AMD provides a direct route from the observed $N_{\text{H}}(\xi)$ trend to the underlying density profile of the flow, $n(r) \propto r^\alpha$ (with $\alpha = (1 + 2m)/(1 + m)$), enabling comparisons with expectations from different wind scenarios and magnetic-wind solutions that predict characteristic radial scalings (e.g. R. D. Blandford & D. G. Payne 1982; J. Contopoulos & R. V. E. Lovelace 1994). The scatter of the open symbols around the filled points then provides a compact visual summary of epoch-to-epoch variability superposed on an underlying ionisation/velocity stratification.

A natural implication is that this multi-phase wind contributes to the long-term obscuration behaviour of Mrk 335. The long-term *Swift*/XRT light curve (Fig. 2) shows that the source spends extended periods in suppressed X-ray states, punctuated by occasional recoveries to higher flux. Variations in the column density and/or covering fraction of a clumpy obscurer crossing the line of sight, while the outflow kinematics remain broadly stable, could account for part of the observed X-ray variability. The similarity between the X-ray and UV outflow velocities further supports an origin at BLR scales, where changes in the projected covering fraction on timescales of days to months are expected. The long-term evolution of the obscurer is discussed further in Section 5.3.

Interestingly, the outflow velocities of these three obscurer components are comparable to the moderately fast, highly ionised winds recently detected in the Fe K band of several Seyfert 1 galaxies (e.g. NGC 4151, MCG-6-30-15) with XRISM (e.g. X. Xiang et al. 2025; L. W. Brenneman et al. 2025). This similarity hints at a possible connection between the soft X-ray obscurer and hotter phases traced by Fe K absorption, suggesting a continuous outflow spanning a broad range of ionisation. A XRISM (M. Tashiro et al. 2025) observation of Mrk 335 would provide a decisive test, as its high spectral resolution in the Fe K band could determine whether the same velocity-stratified outflow extends into the highly ionised regime.

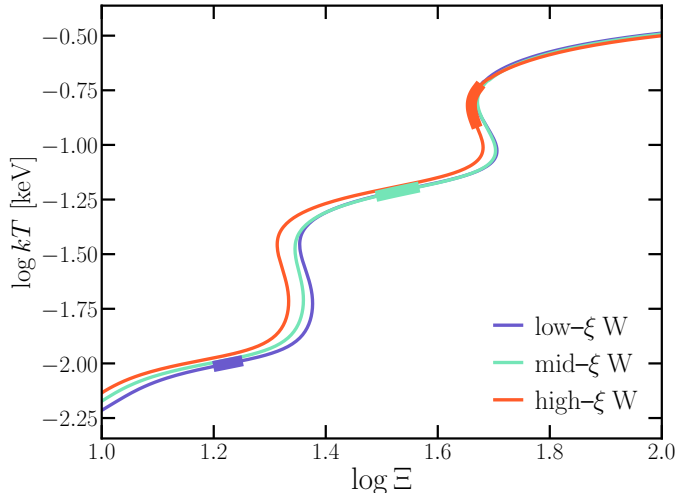


Figure 9. Thermal stability curves (S-curves) for each ionised absorber, computed for the SED seen by each component, and the location of the absorbers assuming thermal equilibrium. Marker sizes reflect the 1σ uncertainty on $\log \xi$.

No statistically significant UFO signature is detected in either the RGS or EPIC-pn spectra, consistent with previous *XMM-Newton* observations of Mrk 335 (e.g. [H. Liu et al. 2021](#)). However, the sensitivity to weak, highly ionised features in the Fe K band is limited with the available data. Future high-resolution spectroscopy with *XRISM* can provide a robust test for transient or weak UFO components, if present, by resolving narrow Fe XXV–Fe XXVI absorption features.

5.1.1. Comparison with other obscurers

A remarkably similar structure of the obscurer studied here was reported in Mrk 817 during the AGN STORM 2 campaign ([F. Zaidouni et al. 2024](#)), with three ionisation components ($\log \xi \approx 2.31, 2.90$, and 3.46), outflow velocities of ~ 3900 – 5900 km s^{-1} , and column densities of order 10^{21} – 10^{22} cm^{-2} . The close resemblance in ionisation structure, column densities, and velocity stratification between Mrk 335 and Mrk 817 suggests a common physical origin for these obscurers ([F. Zaidouni et al. 2024](#)).

By contrast, NGC 3227 shows evidence for a two-phase obscurer during an obscured 2016 observation ([Y. Wang et al. 2022](#)), with $\log \xi \sim 1.0$ and 2.8 . In that case, the stronger absorption hampers sensitivity to higher-ionisation phases and the outflow velocities are not well constrained. Unlike Mrk 335 and Mrk 817, NGC 3227 also hosts multiple persistent, slower warm-absorber components (typical velocities of a few hundred to ~ 1000 km s^{-1}). The apparent absence of classical, long-lived warm absorbers in Mrk 335 and Mrk 817, even during high-flux, nearly unabsorbed states, may indicate that obscuration in these sources is dominated by intermittent BLR-scale disk-wind episodes, rather than occurring on top of a persistent warm-absorber system as in sources such as NGC 5548 and NGC 3227 ([M. Mehdipour et al. 2022](#); [Y. Wang et al. 2022](#)). It will be important to establish whether this difference is driven primarily by geometry (e.g. line-of-sight inclination) or by intrinsic properties of the accreting system (e.g. Eddington ratio, black-hole mass, or SED shape). A follow-up study will explore the population of obscurers in Seyfert 1 galaxies and search for such trends.

5.1.2. Thermal stability

The thermal stability of the absorbers can be assessed using the stability curves shown in Fig. 9. Because the three components are arranged along the line of sight, each absorber sees a different ionising SED owing to shielding by the components closer to the central source; we therefore compute a separate stability curve (S-curve) for each absorber using the corresponding transmitted SED. These curves summarise the thermal equilibrium solutions of photoionised gas: for a given radiation field they indicate which combinations of temperature and ionisation/pressure can be maintained in steady state, and whether small perturbations in temperature will damp out (stable) or run away (unstable). The curves are expressed in terms of the pressure ionisation parameter Ξ , defined as the ratio of radiation pressure to gas pressure, $\Xi = \xi / (4\pi ckT)$ ([J. H. Krolik et al. 1981](#)), where c is the speed of light and kT is the electron temperature. Regions with negative slope on the S-curve correspond to thermally unstable equilibrium, whereas positive slopes indicate thermally stable solutions.

Given the inferred persistence of the obscurer (Sections 5.2 and 5.3), thermal stability is expected. The locations of the three components are consistent with stable (or marginally stable) branches of their respective curves. Notably, the high- ξ component lies close to the turning point where the curve transitions between unstable and stable branches. Gas near this critical point can undergo large temperature/ionisation changes in response to modest variations in the incident ionising flux or shielding, naturally promoting a multi-phase structure in which unstable gas fragments into cooler clumps embedded in a hotter, more tenuous medium (R. C. Dannen et al. 2020). This offers a natural interpretation for the rapid evolution of the high- ξ phase during the campaign: in Epoch 2, the best-fit ionisation parameter decreases (Table 3), consistent with the high- ξ gas moving off the turning point toward a cooler, less ionised equilibrium branch as the incident ionising continuum and/or shielding conditions change.

5.1.3. Testing collisional ionisation

Finally, we tested whether the absorption could be produced by collisionally ionised gas rather than by photoionisation. In some situations, collisionally ionised and photoionised plasmas can produce qualitatively similar sets of absorption lines, especially when only a limited set of ions is detected. Collisionally ionised gas may arise from shocks generated when a fast outflow interacts with slower material, such as previously ejected components or circumnuclear/circumgalactic gas. Recent studies have reported evidence for such collisionally ionised phases in Seyfert 1 galaxies, including NGC 4051, Mrk 1239, and Mrk 766 (A. Ogorzalek et al. 2022; M. Z. Buhariwalla et al. 2023; T. Matamoro Zatarain et al. 2025).

To assess this possibility, we replaced the `pion` components with `hot` components in SPEX (collisional ionisation equilibrium) for both the stacked RGS spectrum and the individual-epoch fits, keeping the overall continuum description unchanged. For each `hot` component, we fitted the column density, temperature, covering fraction, and turbulent and outflow velocities. In all cases, the fits were significantly worse than the corresponding photoionisation models, failing in particular to reproduce the relative strengths of lines from different charge states even when multiple temperature components were allowed. Quantitatively, the best-fit C-statistic increased by $\Delta C \simeq 40\text{--}50$ for each epoch when using collisional models in place of `pion`, for the same number of free parameters.

We also explored hybrid models that include both photoionised (`pion`) and collisionally ionised (`hot`) absorbers. These fits consistently preferred the `pion` components, with the collisional components either unconstrained or driven to negligible column densities. The hybrid fits yield only marginal improvements ($\Delta C \simeq 0\text{--}10$) despite introducing additional free parameters (six in total). We therefore conclude that the obscurer in Mrk 335 is statistically (and physically) better described as photoionised gas, as expected in the presence of the strong AGN radiation field. This interpretation is also consistent with previous analyses of Mrk 335 in obscured/intermediate states (e.g. A. L. Longinotti et al. 2013) and with the long-term behaviour discussed in Section 5.3.

5.2. Short-term Variability of the Obscuring Wind

The five consecutive XMM-Newton pointings provide a unique opportunity to probe the obscuring wind variability on day timescales. The best-fit wind parameters for each epoch are reported in Table 3. To search for correlations, Fig. 7 shows the column density, ionisation parameter, and outflow velocity of all three components as a function of time and of the ionising luminosity L_{ion} (integrated over 1–1000 Ry).

The column densities vary significantly around their time-averaged values. The most prominent change is the drop in N_{H} of the low- ξ component during the flare in Epoch 4. To test whether this change could instead be driven by partial covering, we performed an additional fit in which both N_{H} and f_{cov} were allowed to vary for that component. The fit statistic did not improve, and the two parameters remained consistent within their uncertainties. We therefore interpret the variability as being primarily driven by changes in column density rather than by changes in covering fraction. On day timescales, such N_{H} variations can be produced by a clumpy absorber moving transversely across the line of sight and/or by radiative acceleration during high-flux phases, which can rapidly reshape the line-of-sight column by changing the wind’s velocity field and density/opacity structure. A second drop in column density is seen for the high- ξ component during the faintest observation; however, in this case degeneracies between N_{H} and ξ , together with the low signal-to-noise ratio, limit the robustness of the inferred change.

Interestingly, the flare in Epoch 4 is followed by an increase in outflow velocity in all three components during Epoch 5. This trend suggests that the enhanced radiation field contributes to accelerating the wind. The acceleration appears to scale with ionisation state, being largest for the high- ξ component and smallest for the low- ξ phase. In the same picture, the increased radiation field during the flare can temporarily reduce the opacity of the coldest phase and lower its line-of-sight column density accelerating for instance the absorbing clumps out of the line of sight.

A qualitatively similar behaviour was reported for Mrk 817, where the obscurer column density reached a minimum during a flaring phase in the long monitoring campaign (E. R. Partington et al. 2023). In that case, the available CCD-resolution data did not allow a meaningful test for velocity changes. Our RGS measurements therefore provide an important observational link between a flare-driven decrease in obscuration and a subsequent increase in outflow velocity, supporting a scenario in which radiative driving plays a direct role in shaping the obscurer on day timescales.

During Epoch 2, the high- ξ and mid- ξ components exchange their ionisation parameters: the mid- ξ phase reaches values comparable to the average high- ξ state, while the high- ξ component attains its minimum $\log \xi$. This occurs simultaneously with a decrease in N_{H} of the high- ξ component and an increase in N_{H} of the mid- ξ component, while the outflow velocities remain consistent with their average values within uncertainties. We investigated whether this behaviour could be an artefact of local minima by repeating the fit with a grid of initial conditions for (N_{H}, ξ) and by allowing the covering fractions to vary. None of these tests yielded a statistically significant improvement, supporting the solution reported in Table 3. Nevertheless, Epoch 2 also corresponds to the lowest observed X-ray flux of the campaign, and both N_{H} and ξ are consequently more weakly constrained.

In the right-hand panels of Fig. 7, the high- ξ component shows a positive trend between $\log \xi$ and L_{ion} , indicating that the gas responds to changes in the ionising continuum on day timescales. This is expected if the high- ξ phase is located relatively close to the central engine. The observed change between the lowest and highest flux states, $\Delta \log \xi = 0.37^{+0.21}_{-0.12}$, is consistent with the variation expected from the measured change in L_{ion} (a factor of ~ 3 over the campaign), suggesting that the gas remains close to photoionisation equilibrium. If the response time is shorter than ~ 1 day (comparable to the observation spacing), the implied recombination timescale requires densities $n \gtrsim 5 \times 10^6 \text{ cm}^{-3}$ and distances $\lesssim 0.03 \text{ pc}$ (i.e. $\sim 2 \times 10^4 R_{\text{g}}$ for $M_{\text{BH}} \simeq 2.7 \times 10^7 M_{\odot}$; C. J. Grier et al. 2012). These estimates are order-of-magnitude and depend on the dominant ions controlling the recombination time and on the assumed SED.

For the mid- ξ component, any trend with L_{ion} is less conclusive, largely due to the outlying point during the faintest observation and the associated large uncertainties. The low- ξ component does not show a clear instantaneous correlation with L_{ion} , but the time evolution suggests a possible delayed response of order ~ 1 day: $\log \xi$ decreases during Epoch 4 after the lower ionising flux in Epoch 3 and increases again in Epoch 5 following the flare. A one-day lag has also been inferred for the obscurer in Mrk 817 from high-cadence NICER monitoring (E. R. Partington et al. 2023). If such a delay is real in Mrk 335, it would place the low- ξ phase further out than the high- ξ component, at distances of order $\sim 0.1 \text{ pc}$ ($\sim 10^5 R_{\text{g}}$). This inference remains tentative, however, because the gaps between observations limit our knowledge of the full ionising-flux history, introducing uncertainty in any lag estimate. The sparse sampling also prevents a robust time-dependent photoionisation analysis (e.g. D. Rogantini et al. 2022b), which would otherwise provide direct constraints on the gas density and distance.

Overall, the day-timescale X-ray variability of Mrk 335 is driven by a combination of intrinsic continuum changes (i.e. variations in the ionising SED) and variable absorption (i.e. changes in the transmission spectrum; see also Fig. 6). The strong day-scale changes in column density (top panels of Fig. 7) support a clumpy outflow geometry. Although N_{H} variations are favoured, changes in covering fraction cannot be excluded, especially for the higher-ionisation components where the $N_{\text{H}}-f_{\text{cov}}$ degeneracy is difficult to break.

To compare intrinsic and absorption-driven variability in an empirical, model-agnostic way, we combined our simplified SED approach with the RGS modelling of the obscuring wind and decomposed the band-limited observed flux as $F_{\text{obs}} = F_{\text{int}} T$, where F_{int} is the unabsorbed continuum flux in our baseline description and $T \equiv F_{\text{obs}}/F_{\text{int}}$ is the corresponding effective transmission. Here T quantifies only the attenuation produced by the three photoionised wind components included in our RGS model; it does not include any additional neutral/low-ionisation partial-covering absorption that may be required in alternative broadband interpretations. This decomposition is intended purely as an empirical diagnostic to separate changes in the baseline continuum from line-of-sight attenuation within our adopted parametrisation; it does not, by itself, identify the physical origin of the variability (e.g. intrinsic coronal changes, relativistic reflection, and/or partial-covering absorption). Between two epochs a and b this gives $\Delta \ln F_{\text{obs}} = \Delta \ln F_{\text{int}} + \Delta \ln T$. In the 0.3–10 keV band, F_{int} varies by a factor $\simeq 3.3$ across the epochs, spanning $F_{\text{int}} \simeq (0.91\text{--}3.00) \times 10^{-11} \text{ erg cm}^{-2} \text{ s}^{-1}$. Over the same period, T spans $\simeq 0.54\text{--}0.80$ (a factor $\simeq 1.5$), indicating that, within this parametrisation, changes in the baseline continuum level appear to dominate the broadband variability, while attenuation by the modelled wind provides an additional, non-negligible modulation.

5.3. Long-term Variability of the Obscuring Wind

Across 15 XMM-Newton observations spanning ~ 20 years (Dec 2000–Jul 2021; total exposure ~ 1.4 Ms), Mrk 335 displays dramatic transitions between spectral states, from bright, weakly absorbed epochs to faint states in which the continuum is strongly suppressed and the spectrum becomes line dominated. Proposed explanations include intrinsic changes in the coronal continuum (M. L. Parker et al. 2014; D. R. Wilkins & L. C. Gallo 2015; L. C. Gallo et al. 2018) and variable absorption along the line of sight (S. Komossa et al. 2020). Disentangling these scenarios requires more accurate continuum modelling, including complex state-of-the-art reflection models and multi-component low-ionisation/neutral partial-covering absorption. In the following, we focus on the wind and obscuration properties in the broader context of the long-term X-ray/UV behaviour, while remaining agnostic about the physical driver of the observed variability.

5.3.1. High-flux, weak-absorption state (2000–2006).

During the first three XMM-Newton observations (2000 and 2006), Mrk 335 was in a high-flux state with a 0.3–10 keV observed flux of $\sim 5 \times 10^{-11}$ erg cm $^{-2}$ s $^{-1}$ (A. L. Longinotti et al. 2008). In this state, only a tenuous ionised outflow was detected, with $\log \xi \sim 1.2$ and $N_{\text{H}} \sim 10^{19}$ cm $^{-2}$ (H. Liu et al. 2021). The outflow velocity changed between the two epochs, increasing in magnitude from ~ 2500 km s $^{-1}$ in 2000 to ~ 7500 km s $^{-1}$ in 2006.

5.3.2. Onset of strong obscuration (2007).

In 2007, Swift caught Mrk 335 in a low-flux state that lasted for at least two months (D. Grupe et al. 2007), with the observed X-ray flux dropping by about an order of magnitude. The contemporaneous RGS spectrum revealed prominent soft X-ray emission lines (e.g. A. L. Longinotti et al. 2008). By comparison with the earlier high-state spectra, D. Grupe et al. (2008) showed that the main spectral changes occurred below 2 keV and that both a reflection-dominated scenario and a partial-covering model (compact clumps obscuring the X-ray source along the line of sight) can reproduce the 2007 spectrum. Using photoionisation modelling, H. Liu et al. (2021) detected a low-ionisation absorber with $\log \xi \sim 0.7$ and $N_{\text{H}} \sim 2 \times 10^{20}$ cm $^{-2}$ outflowing at $v_{\text{out}} \sim -6500$ km s $^{-1}$.

5.3.3. Intermediate-flux state and emergence of a multi-phase obscurer (2009).

Two consecutive XMM-Newton orbits in 2009 (total exposure of ~ 200 ks) captured Mrk 335 in an intermediate-flux state ($F_{0.3-10 \text{ keV}} \sim 10^{-11}$ erg cm $^{-2}$ s $^{-1}$) and revealed a complex ionised wind (A. L. Longinotti et al. 2013). The high-resolution grating spectra required three distinct ionised components, all outflowing at relatively high velocities of $(4-6) \times 10^3$ km s $^{-1}$. Notably, the presence of a variable, complex ionised absorber had already been proposed to explain the peculiar 1987 Ginga spectrum (T. J. Turner et al. 1993), for which an ionised absorber with $N_{\text{H}} \sim 10^{22}$ cm $^{-2}$ was invoked.

The physical parameters of the 2009 wind, ionisation states ($\log \xi \sim 1.8, 2.1, 3.3$) and column densities ($N_{\text{H}} \sim 10^{21-22}$ cm $^{-2}$), are broadly consistent with those measured in our 2021 campaign, strongly suggesting that the same phenomenology recurs in Mrk 335 across decade timescales. The ionisation parameters reported in A. L. Longinotti et al. (2013) are slightly lower than in 2021, which may reflect differences in the assumed SED and/or photoionisation modelling choices (see e.g. M. Mehdipour et al. 2016 for the impact of SED and code differences). Nevertheless, their transmission spectra show the same qualitative requirements: a low-ionisation component is needed to reproduce the Fe UTA, and multiple components are required to fit high-ionisation lines such as O VIII. In 2009 the outflow velocities of the low- and mid-ionisation phases were higher (~ 4000 and ~ 5100 km/s respectively) than those we measure in 2021 for the corresponding components, which may indicate intrinsic variability in the wind kinematics and is consistent with the short-term velocity changes we observe during the 2021 flare.

5.3.4. Deep low-flux states and line-dominated spectra (2015–2019).

The 2009 intermediate-state observation was followed by four XMM-Newton Target-of-Opportunity observations (2015, 2018, and early and late 2019) that captured Mrk 335 in its lowest X-ray flux states (A. L. Longinotti et al. 2019; M. L. Parker et al. 2019; H. Liu et al. 2021). During these epochs, the grating spectra are dominated by strong photoionised emission lines, together with an ionised absorber characterised by $\log \xi \approx 1.3-1.5$, $N_{\text{H}} \approx 10^{20-21}$ cm $^{-2}$, and $v_{\text{out}} \approx -5700$ km s $^{-1}$. For the 2018–2019 observations, two emission components ($\log \xi \sim 1.0$ and 2.4, with $n_{\text{H}} \sim 10^6$ cm $^{-3}$) were required to reproduce the rich line forest (M. L. Parker et al. 2019). The higher-ionisation component was not detected during these low-flux epochs; it may nevertheless be present, with the limited signal-to-noise ratio preventing a robust detection.

The O VII triplet displayed dramatic changes in line ratios between 2018 and 2019: in 2018 the resonance line dominated, whereas in 2019 the forbidden line became the strongest. [M. L. Parker et al. \(2019\)](#) interpreted this change as the result of a lower ionisation state and stronger attenuation of the resonance line, implying an extended scattering/emitting region ($r \gtrsim 0.1$ pc) rather than BLR-scale gas. By contrast, the 2007 low-flux observation showed an O VII triplet dominated by the intercombination line, consistent with much higher densities ($n_{\text{H}} \sim 10^{10-11} \text{ cm}^{-3}$; [A. L. Longinotti et al. 2008](#)). These differences suggest that the line-dominated spectra in 2018–2019 do not necessarily share the same physical origin as the soft X-ray emission observed in 2007.

5.3.5. UV connection and multiwavelength perspective.

Multiple HST observations of Mrk 335 between 1994 and 2018 reveal strong, broad, blueshifted absorption in Ly α and C VI ([A. L. Longinotti et al. 2013, 2019](#)). In 2009, the UV absorption troughs ($v_{\text{out}} \sim -6500 \text{ km s}^{-1}$, $FWHM \sim 2600 \text{ km s}^{-1}$) had velocities comparable to the X-ray absorption features in the contemporaneous intermediate-flux XMM-Newton data. [A. L. Longinotti et al. \(2013\)](#) also reported substantial variability of the C VI absorption on month-to-year timescales, consistent with column-density changes driven by bulk motion, underscoring the diagnostic power of combining high-resolution UV and X-ray spectroscopy.

Two quasi-simultaneous HST/COS and XMM-Newton campaigns were performed in 2015/2016 and 2018. In 2015/2016, the outflow velocities inferred in the two bands were remarkably consistent ($v_{\text{out,X}} \sim 5700 \text{ km s}^{-1}$ and $v_{\text{out,UV}} \sim 5200 \text{ km s}^{-1}$, with $FWHM \sim 700 \text{ km s}^{-1}$; [A. L. Longinotti et al. 2019](#)). While the soft X-ray absorber covered nearly the entire X-ray source ($C_{\text{f,X}} \approx 1$), the UV absorber covered only ~ 20 – 30% of the ionising continuum, suggesting either a more extended UV-emitting region and/or strong inhomogeneity in the absorber. In 2018 the broad UV absorption remained visible, but its velocity decreased to $\sim 3000 \text{ km s}^{-1}$, while the X-ray outflow maintained a higher velocity ([M. L. Parker et al. 2019](#)), indicating that the UV and X-ray absorbing zones can evolve differently even when they are likely related.

5.3.6. Implications: a recurring, clumpy obscurer.

The long-term behaviour of Mrk 335 therefore supports a picture in which a multi-phase, moderately fast obscuring wind is an intrinsic component of the accretion flow, recurring on decade timescales rather than arising from a transient external absorber. The similarity between the 2009 and 2021 intermediate-state spectra implies that the wind can maintain a broadly similar ionisation/velocity stratification over $\gtrsim 10$ yr. During the lowest-flux XMM-Newton observations, only the low- ξ component is detected ([H. Liu et al. 2021](#)); the limited signal-to-noise and the strong suppression of the soft continuum prevent a meaningful search for weaker, higher-ionisation features. The absence of the mid- and high- ξ phases in these spectra therefore does not necessarily imply that they are physically absent. Instead, a simple interpretation is that the same multi-phase outflow persists, while variations in the line-of-sight covering fraction and/or total column density—and, potentially, changes in the intrinsic continuum level—modulate both the observed flux and the detectability of the more highly ionised components. This is consistent with the intermediate-state epochs, where the higher-ionisation phases re-emerge as the continuum recovers.

5.4. Origin

Classical warm absorbers in Seyfert 1 galaxies are typically inferred to arise on scales of ~ 0.1 pc to ~ 1 kpc and have characteristic outflow velocities of a few hundred to $\sim 10^3 \text{ km s}^{-1}$. In Mrk 335, the three photoionised absorbers detected in the intermediate-flux state have substantially higher velocities ($|v_{\text{out}}| \simeq 2150$ – 5900 km s^{-1} ; Table 3), pointing to an origin closer to the accretion flow/BLR region and disfavoring a torus-scale location. The similarity in ionisation structure and kinematics with the obscurer in Mrk 817 ([F. Zaidouni et al. 2024](#)) further suggests that clumpy, multi-phase obscurers may represent a common phenomenon in Seyfert 1 galaxies. To enable a direct comparison with Mrk 817, we follow the same order-of-magnitude arguments of [F. Zaidouni et al. \(2024\)](#) to constrain the location (and, below, the energetics) of the outflow.

5.4.1. Distance

Upper limit from thickness arguments.—An upper limit on the distance can be obtained by requiring that the absorber thickness (Δr) does not exceed its distance from the source, $\Delta r/r < 1$. Using $N_{\text{H}} \sim n C_{\text{v}} \Delta r$ and substituting $n = L_{\text{ion}}/(\xi r^2)$ gives

$$r_{\text{max}} \simeq \frac{L_{\text{ion}}}{N_{\text{H}} \xi}, \quad (1)$$

where $C_v < 1$ is a volume-filling factor. Using the average ionising luminosity from the SED modelling (Table 2, $L_{\text{ion}} \simeq 1.5 \times 10^{44}$ erg s $^{-1}$) yields $r_{\text{max}} \sim 0.09$ pc for the high- ξ component and $r_{\text{max}} \sim 2$ pc for the mid- ξ component. For the low- ξ component, this constraint is comparatively weak (~ 300 pc) because of its smaller ξ and N_{H} . These limits are conservative, since C_v is expected to be well below unity in a clumpy wind. In addition, the differences in the transmitted ionising luminosity seen by the individual components are modest (\lesssim a few per cent), so adopting the average L_{ion} is sufficient for these order-of-magnitude estimates.

A characteristic radius can be estimated by assuming that the measured outflow velocity is comparable to the local escape velocity, $v_{\text{out}} \approx v_{\text{esc}} = \sqrt{2GM_{\text{BH}}/r}$. This provides only an order-of-magnitude reference: the wind need not move at the escape speed, since it may be a failed wind (with a total velocity below v_{esc}) or, conversely, a successful wind whose total velocity exceeds v_{esc} , while the observed line-of-sight component depends on geometry. Under this assumption,

$$\frac{r}{R_{\text{g}}} \simeq 2 \left(\frac{c}{|v_{\text{out}}|} \right)^2, \quad (2)$$

where $R_{\text{g}} = GM_{\text{BH}}/c^2$. Adopting $M_{\text{BH}} = 2.7 \times 10^7 M_{\odot}$ (C. J. Grier et al. 2012), we obtain $r \simeq 5.2 \times 10^3 R_{\text{g}}$ ($\simeq 6.7 \times 10^{-3}$ pc) for the high- ξ component ($|v_{\text{out}}| \simeq 5900$ km s $^{-1}$), $r \simeq 1.8 \times 10^4 R_{\text{g}}$ ($\simeq 2.3 \times 10^{-2}$ pc) for the mid- ξ component ($|v_{\text{out}}| \simeq 3200$ km s $^{-1}$), and $r \simeq 3.9 \times 10^4 R_{\text{g}}$ ($\simeq 5.0 \times 10^{-2}$ pc) for the low- ξ component ($|v_{\text{out}}| \simeq 2150$ km s $^{-1}$). These radii lie naturally on BLR scales.

Using the kinematic estimate for the low- ξ component, the implied number density is $n \sim 5 \times 10^7$ cm $^{-3}$. At this density, the recombination timescales of the dominant XMM-Newton/RGS ions (e.g. O VII–O VIII, Ne IX–Ne X, and the Fe UTA/L-shell ions) are short, of order hours. A ~ 1 day response would instead require a lower density, $n \sim 5 \times 10^6$ cm $^{-3}$, implying a larger distance ($r \sim 0.1$ – 0.2 pc) for the low- ξ phase. If the tentative ~ 1 -day delay of the low- ξ component is confirmed (see Section 5.2), the absorber would lie beyond the escape-radius estimate, disfavouring a failed-wind interpretation.

F. Zaidouni et al. (2024) used short-timescale variability and an assumed compact corona of size $R_{\text{c}} \sim 10 R_{\text{g}}$ to estimate a transverse velocity $v_{\perp} \gtrsim R_{\text{c}}/\delta t$, and (assuming Keplerian motion) infer $r/R_{\text{g}} \sim (c/v_{\perp})^2$. Here δt denotes the characteristic timescale over which a significant change in the absorber is observed (e.g. in N_{H} and/or ξ), interpreted as the time required for a clump to traverse a distance comparable to the projected size of the X-ray corona. In Mrk 335, the strongest absorber changes occur on day timescales across the five epochs (Section 5.2). Note that the clump does not have to cross the entire X-ray source size, just a significant portion of it. For $\delta t \sim 1$ day and $R_{\text{c}} \sim 10 R_{\text{g}}$, the implied transverse velocity is $v_{\perp} \sim 4600$ km s $^{-1}$, corresponding to

$$r \sim 4 \times 10^3 R_{\text{g}} \simeq 5 \times 10^{-3} \text{ pc}. \quad (3)$$

This estimate is consistent with the escape-velocity radii above and points to a location comparable to the characteristic H β BLR radius of Mrk 335, $R_{\text{BLR}} \simeq 14$ light-days $\approx 10^4 R_{\text{g}}$ (C. J. Grier et al. 2012). Given the sparse sampling, it should be regarded as indicative.

Taken together, these arguments place the obscurer within $\sim 10^{-3}$ – 10^{-1} pc ($\sim 10^3$ – $10^5 R_{\text{g}}$), with the high- ξ phase located closest to the black hole and the low- ξ component further out. This ordering is consistent with the short-term variability trends (Section 5.2), where the high- ξ component responds most directly to changes in L_{ion} , while the low- ξ phase shows at most a delayed response. Our inferred distance range is broadly consistent with the interpretation of the 2009 intermediate-flux state in A. L. Longinotti et al. (2013), who also reported kinematic consistency between the UV and X-ray absorbers on BLR-like scales. The distances inferred here are also comparable to those obtained for Mrk 817 by F. Zaidouni et al. (2024), which is particularly notable given the similar black-hole masses of the two systems (for Mrk 817, $\log(M_{\text{BH}}/M_{\odot}) = 7.59$; M. C. Bentz & E. Manne-Nicholas 2018).

5.4.2. Energetics

Following F. Zaidouni et al. (2024), we estimate the mass outflow rate and kinetic power of the obscurer with simple continuity arguments. For a radial outflow subtending a solid angle Ω , the mass flux is $\dot{M} = \Omega r^2 \rho v$, where v is the outflow velocity and $\rho = C_v m_{\text{p}} n$ is the mass density (with particle density n , proton mass m_{p} , and volume-filling factor $C_v < 1$). The observed column density is $N_{\text{H}} \simeq n C_v \Delta r$, where Δr is the absorber thickness.

Requiring that the absorber is not geometrically thicker than its distance from the source ($\Delta r < r$) gives a lower limit on the mass outflow rate per unit solid angle that is independent of C_v ,

$$\left(\frac{\dot{M}_{\min}}{\Omega}\right)_{\text{tot}} \gtrsim m_p \sum_i r_i N_{\text{H},i} |v_i| \simeq 5.6 \times 10^{-2} M_{\odot} \text{ yr}^{-1} \text{ sr}^{-1}, \quad (4)$$

where the sum runs over the three pion components, using their time-averaged N_{H} and v_{out} (Table 3). A characteristic radius for each phase is assigned using the escape-velocity estimate (Section 5.4.1), $r_i/R_g \simeq 2(c/|v_i|)^2$. This mapping is uncertain because the true 3D velocity field and geometry are not directly measured.

The corresponding minimum kinetic luminosity follows from $L_{\text{kin}} = \frac{1}{2}\dot{M}v^2$:

$$\left(\frac{L_{\text{kin},\min}}{\Omega}\right)_{\text{tot}} \gtrsim \frac{1}{2}m_p \sum_i r_i N_{\text{H},i} |v_i|^3 \simeq 4.9 \times 10^{41} \text{ erg s}^{-1} \text{ sr}^{-1} \simeq 0.084\% L_{\text{bol}} \Omega^{-1}, \quad (5)$$

where $L_{\text{bol}} = 5.86 \times 10^{44} \text{ erg s}^{-1}$ is calculated from our unobscured SED model integrated over 10^{-3} – 10^5 eV .

An upper-limit scaling can be obtained by eliminating n using the ionisation parameter $\xi = L_{\text{ion}}/(nr^2)$ (A. J. Blustin et al. 2005). This yields, for each phase, $\dot{M}/(C_v\Omega) \simeq m_p L_{\text{ion}}|v|/\xi$, and therefore

$$\left(\frac{L_{\text{kin}}}{C_v\Omega}\right)_{\text{tot}} \simeq \frac{1}{2}m_p L_{\text{ion}} \sum_i \frac{|v_i|^3}{\xi_i} \simeq 2.2 \times 10^{43} \text{ erg s}^{-1} \text{ sr}^{-1} \simeq 3.8\% L_{\text{bol}} \Omega^{-1} C_v^{-1}, \quad (6)$$

using time-averaged ξ_i and $|v_i|$ from Table 3 and $L_{\text{ion}} = 1.54 \times 10^{44} \text{ erg s}^{-1}$ (Table 2).

We adopt a fiducial global covering factor $\Omega/4\pi = 0.25$ (i.e. $\Omega = \pi$). The volume-filling factor is unknown; within the upper-limit scaling, a conservative bound is obtained by taking $C_v = 1$. For these assumed values, we obtain $0.26\% \lesssim L_{\text{kin}}/L_{\text{bol}} \lesssim 12\%$. More realistically, if $C_v \lesssim 0.08$ as inferred for Seyfert warm absorbers (A. J. Blustin et al. 2005), the scaling gives $L_{\text{kin}}/L_{\text{bol}} \lesssim 0.94\%$. Comparing with the commonly adopted feedback threshold $L_{\text{kin}}/L_{\text{bol}} \sim 0.5\%$ (P. F. Hopkins & M. Elvis 2010), often used as an approximate criterion for an outflow to carry enough kinetic power to affect the host galaxy on large scales, the upper-limit scaling exceeds this threshold for $C_v \gtrsim 0.042$ (for $\Omega = \pi$), while the lower bound already requires $L_{\text{kin}}/L_{\text{bol}} \gtrsim 0.26\%$. This might suggest that the obscurer in Mrk 335 could be energetically significant for AGN feedback, depending on its global covering and clumpiness.

These energetics are similar to those inferred for Mrk 817 (F. Zaidouni et al. 2024). We stress, however, that they remain uncertain because they depend on the poorly constrained global geometry (Ω) and volume filling factor (C_v), as well as on the simplifying assumptions used to relate velocity to radius in the lower-limit estimate. Moreover, the kinetic power inferred here is based on a limited number of epochs and may not represent the long-term duty cycle of the obscurer.

5.5. Emission lines

The RGS spectrum of Mrk 335 shows clear signatures of multiple narrow emission lines. The strongest features are H-like and He-like transitions of C, N, and O, which likely originate in photoionised gas on scales larger than the immediate vicinity of the X-ray source (e.g. the narrow-line region and/or an extended outflow). These emission lines dominated the RGS spectrum during previous low-flux/obscured observations in 2015 and 2018/2019, and they are also detected in the intermediate-flux observations in 2007 and 2009. In the high-flux states in 2000 and 2006 they are only weakly detected, primarily because the strong continuum reduces the line contrast.

In detailed analyses of the 2018–2019 low-state spectra, M. L. Parker et al. (2019) and H. Liu et al. (2021) modelled the emission features with two photoionised emission components with ionisation parameters of $\log \xi \simeq 0.2$ – 1.3 and $\log \xi \simeq 1.4$ – 2.4 . They found that the emission components vary in ionisation state and flux across epochs, and are blueshifted with respect to the systemic frame, with velocities ranging from $\sim 100 \text{ km s}^{-1}$ in observations after 2015 up to a few thousand km s^{-1} in earlier epochs.

In this work, our primary focus is the obscurer seen in absorption. To keep the fits computationally efficient, we model the emission lines phenomenologically with Gaussian profiles, following the approach of A. L. Longinotti et al. (2013), rather than using a full photoionisation emission calculation with pion. As a consistency check, we performed exploratory fits including photoionised emission components and found that two phases with $\log \xi \sim 1.0$ and ~ 2.3 are required to reproduce the line spectrum, broadly consistent with previous work. A dedicated analysis of the emission-line plasma, including self-consistent photoionisation emission modelling, is deferred to future work.

The full list of detected emission lines is given in Table 4. The Ly α and He α emission lines of carbon, nitrogen, and oxygen are relatively narrow, with FWHM $\lesssim 0.2 \text{ \AA}$. The main exception is N VII Ly α , whose fitted width is larger; this feature is likely affected by blending with the recombination-continuum C VI structure (e.g. M. L. Parker et al. 2019). In addition, the O VIII and C VI Ly α lines show broad residual emission underlying the narrow cores. We modelled these residuals by adding broad Gaussian components centred at the corresponding reference wavelengths. The origin of these broad components (FWHM $\sim 3\text{--}4 \text{ \AA}$) is uncertain. One possibility is that they trace reprocessed emission from the inner accretion flow (e.g. relativistically broadened disc emission), although our spectral setup does not include a self-consistent soft X-ray reflection model that could test this scenario. Alternative explanations include Compton broadening in an optically thick scattering region.

In the individual-epoch fits, we allowed only the line normalisations to vary, while the line centroids and widths were fixed to their values from the stacked spectrum. We find that the line normalisations vary significantly between epochs. If the dominant emission originates at large radii, such variability on day timescales would be unexpected and may instead reflect changes in the underlying continuum/absorption affecting the inferred line fluxes, or a contribution from a more compact emitting/scattering region. We leave a detailed investigation of the emission-line variability to future work, where we will model the full line forest with photoionisation emission codes.

6. CONCLUSION

We presented results from a coordinated XMM-*Newton*/NuSTAR campaign on Mrk 335 in June 2021, complemented by long-term *Swift* monitoring. The source was observed in an intermediate-flux state, enabling a detailed high-resolution study of the ionised obscurer with the RGS and, for the first time in Mrk 335, a time-resolved characterisation of its variability on day timescales. Our main results are:

- *Three-phase obscurer.* The stacked RGS spectrum reveals three photoionised absorption components with time-averaged ionisation parameters of $\log \xi \simeq 3.63$ (high- ξ), 3.10 (mid- ξ), and 2.01 (low- ξ), outflowing at $|v_{\text{out}}| \simeq 5900$, 3200, and 2150 km s $^{-1}$, respectively. Their ionisation structure and column densities are broadly consistent with those inferred during the intermediate-flux XMM-*Newton* observation in 2009 (A. L. Longinotti et al. 2013), suggesting that similar multi-phase obscuration recurs in Mrk 335 over decade timescales.
- *Day-scale variability and clumpiness.* Across the five consecutive RGS spectra, all three phases vary in column density and ionisation parameter, and show changes in outflow velocity. The strong day-scale changes in N_{H} and transmission favour a clumpy, inhomogeneous obscurer rather than a uniform screen.
- *Flare-associated changes.* The most prominent event is an extreme drop in column density of the low- ξ absorber component during the flare in Epoch 4, consistent with a rapid decrease in line-of-sight opacity. Together with the velocity increase observed in Epoch 5, this behaviour is consistent with the enhanced radiation field modifying the wind structure and possibly contributing to radiative acceleration, particularly for the coldest phase.
- *Different response times across phases.* The high- ξ component shows the clearest response to changes in the ionising luminosity, consistent with a location closer to the central engine than the lower-ionisation phases. The low- ξ component shows at most a delayed response of order ~ 1 day, which, if confirmed with denser sampling, would place it further out.
- *What drives the X-ray variability.* Broadband modelling shows that the X-ray variability in the intermediate state is driven by both intrinsic continuum variability and variable absorption. The wind transmission changes mainly through variations in N_{H} , while the hard X-ray band traces changes in the coronal continuum. The tendency for the low- ξ column density to decrease during high-luminosity phases suggests that radiative driving may play an important role in shaping the coldest phase.
- *Location and energetics.* Our order-of-magnitude distance estimates place the obscurer at BLR scales, spanning $\sim 10^3\text{--}10^5 R_{\text{g}}$, comparable to (and partly interior to) the characteristic BLR radius of Mrk 335. Depending on the global geometry and clumpiness, the inferred kinetic power can reach the percent level of L_{bol} , implying that such obscurers may contribute to feedback on the host galaxy.

Future high-cadence, simultaneous UV–X-ray monitoring combined with time-dependent photoionisation modelling will be essential to test these distance estimates directly by measuring the absorber number density from its response to continuum variability.

ACKNOWLEDGMENTS

D.R. is grateful to Jelle de Plaa and Liyi Gu for their support and assistance with the SPEX software. During the project, D.R. received support from the Margaret Burbidge Fellowship supported by the Brinson Foundation as well as the NASA through the Smithsonian Astrophysical Observatory (SAO) contract SV3-73016 to MIT for Support of the Chandra X-Ray Center (CXC) and Science Instruments. P.K. is supported by NASA through the NASA Hubble Fellowship grant HST-HF2-51534.001-A awarded by the Space Telescope Science Institute, which is operated by the Association of Universities for Research in Astronomy, Incorporated, under NASA contract NAS5-26555. E.B. is supported by The Israel Science Foundation (grant No. 2617/25). This research is partly based on observations obtained with XMM-Newton, an ESA science mission with instruments and contributions directly funded by ESA Member States and NASA.

Facilities: Swift(XRT and UVOT), XMM-Newton (RGS, EPIC-pn), NuSTAR

Software: SPEX (J. S. Kaastra et al. 2020)

REFERENCES

- Audard, M., Awaki, H., Ballhausen, R., et al. 2025, *Nature*, doi: [10.1038/s41586-025-08968-2](https://doi.org/10.1038/s41586-025-08968-2)
- Behar, E. 2009, *ApJ*, 703, 1346, doi: [10.1088/0004-637X/703/2/1346](https://doi.org/10.1088/0004-637X/703/2/1346)
- Behar, E., Sako, M., & Kahn, S. M. 2001, *ApJ*, 563, 497, doi: [10.1086/323966](https://doi.org/10.1086/323966)
- Behar, E., Peretz, U., Kriss, G. A., et al. 2017, *A&A*, 601, A17, doi: [10.1051/0004-6361/201629943](https://doi.org/10.1051/0004-6361/201629943)
- Bentz, M. C., & Manne-Nicholas, E. 2018, *ApJ*, 864, 146, doi: [10.3847/1538-4357/aad808](https://doi.org/10.3847/1538-4357/aad808)
- Bentz, M. C., Denney, K. D., Grier, C. J., et al. 2013, *ApJ*, 767, 149, doi: [10.1088/0004-637X/767/2/149](https://doi.org/10.1088/0004-637X/767/2/149)
- Bianchi, S., Matt, G., Haardt, F., et al. 2001, *A&A*, 376, 77, doi: [10.1051/0004-6361:20010971](https://doi.org/10.1051/0004-6361:20010971)
- Blandford, R. D., & Payne, D. G. 1982, *MNRAS*, 199, 883, doi: [10.1093/mnras/199.4.883](https://doi.org/10.1093/mnras/199.4.883)
- Blustin, A. J., Page, M. J., Fuerst, S. V., Branduardi-Raymont, G., & Ashton, C. E. 2005, *A&A*, 431, 111, doi: [10.1051/0004-6361:20041775](https://doi.org/10.1051/0004-6361:20041775)
- Brenneman, L. W., Wilkins, D. R., Ogorzałek, A., et al. 2025, arXiv e-prints, arXiv:2510.08926, doi: [10.48550/arXiv.2510.08926](https://doi.org/10.48550/arXiv.2510.08926)
- Buhariwalla, M. Z., Gallo, L. C., Mao, J., et al. 2023, *MNRAS*, 521, 2378, doi: [10.1093/mnras/stad265](https://doi.org/10.1093/mnras/stad265)
- Burrows, D. N., Hill, J. E., Nousek, J. A., et al. 2005, *SSRv*, 120, 165, doi: [10.1007/s11214-005-5097-2](https://doi.org/10.1007/s11214-005-5097-2)
- Cardelli, J. A., Clayton, G. C., & Mathis, J. S. 1989, *ApJ*, 345, 245, doi: [10.1086/167900](https://doi.org/10.1086/167900)
- Contopoulos, J., & Lovelace, R. V. E. 1994, *ApJ*, 429, 139, doi: [10.1086/174307](https://doi.org/10.1086/174307)
- Crummy, J., Fabian, A. C., Gallo, L., & Ross, R. R. 2006, *MNRAS*, 365, 1067, doi: [10.1111/j.1365-2966.2005.09844.x](https://doi.org/10.1111/j.1365-2966.2005.09844.x)
- Dannen, R. C., Proga, D., Waters, T., & Dyda, S. 2020, *ApJL*, 893, L34, doi: [10.3847/2041-8213/ab87a5](https://doi.org/10.3847/2041-8213/ab87a5)
- De Rosa, G., Peterson, B. M., Ely, J., et al. 2015, *ApJ*, 806, 128, doi: [10.1088/0004-637X/806/1/128](https://doi.org/10.1088/0004-637X/806/1/128)
- den Herder, J. W., Brinkman, A. C., Kahn, S. M., et al. 2001, *A&A*, 365, L7, doi: [10.1051/0004-6361:20000058](https://doi.org/10.1051/0004-6361:20000058)
- Detmers, R. G., Kaastra, J. S., Steenbrugge, K. C., et al. 2011, *A&A*, 534, A38, doi: [10.1051/0004-6361/201116899](https://doi.org/10.1051/0004-6361/201116899)
- Done, C., Davis, S. W., Jin, C., Blaes, O., & Ward, M. 2012, *MNRAS*, 420, 1848, doi: [10.1111/j.1365-2966.2011.19779.x](https://doi.org/10.1111/j.1365-2966.2011.19779.x)
- Ebrero, J., Kriss, G. A., Kaastra, J. S., & Ely, J. C. 2016, *A&A*, 586, A72, doi: [10.1051/0004-6361/201527495](https://doi.org/10.1051/0004-6361/201527495)
- Evans, P. A., Beardmore, A. P., Page, K. L., et al. 2007, *A&A*, 469, 379, doi: [10.1051/0004-6361:20077530](https://doi.org/10.1051/0004-6361:20077530)
- Evans, P. A., Beardmore, A. P., Page, K. L., et al. 2009, *MNRAS*, 397, 1177, doi: [10.1111/j.1365-2966.2009.14913.x](https://doi.org/10.1111/j.1365-2966.2009.14913.x)
- Fürst, F. 2022, Empirical correction of the EPIC effective area based on NuSTAR observations, Tech. Rep. XMM-SOC-CAL-TN-0230, European Space Agency - XMM-Newton Calibration Technical Note
- Gallo, L. 2018, in *Revisiting Narrow-Line Seyfert 1 Galaxies and their Place in the Universe*, 34. <https://arxiv.org/abs/1807.09838>
- Gallo, L. C., Blue, D. M., Grupe, D., Komossa, S., & Wilkins, D. R. 2018, *Monthly Notices of the Royal Astronomical Society*, 478, 2557, doi: [10.1093/mnras/sty1134](https://doi.org/10.1093/mnras/sty1134)
- Gallo, L. C., Gonzalez, A. G., & Miller, J. M. 2021, *ApJL*, 908, L33, doi: [10.3847/2041-8213/abdc5](https://doi.org/10.3847/2041-8213/abdc5)

- Gallo, L. C., Miller, J. M., & Costantini, E. 2023, in High-Resolution X-ray Spectroscopy: Instrumentation, ed. C. Bambi & J. Jiang, 209–254, doi: [10.1007/978-981-99-4409-5_9](https://doi.org/10.1007/978-981-99-4409-5_9)
- Gallo, L. C., Gonzalez, A. G., Waddell, S. G. H., et al. 2019, MNRAS, 484, 4287, doi: [10.1093/mnras/stz274](https://doi.org/10.1093/mnras/stz274)
- García, J., Dauser, T., Reynolds, C. S., et al. 2013, ApJ, 768, 146, doi: [10.1088/0004-637X/768/2/146](https://doi.org/10.1088/0004-637X/768/2/146)
- Gehrels, N., Chincarini, G., Giommi, P., et al. 2004, ApJ, 611, 1005, doi: [10.1086/422091](https://doi.org/10.1086/422091)
- Gonzalez, A. G., Gallo, L. C., Miller, J. M., et al. 2024, MNRAS, 527, 5569, doi: [10.1093/mnras/stad3549](https://doi.org/10.1093/mnras/stad3549)
- Grafton-Waters, S., Mao, J., Mehdipour, M., et al. 2023, A&A, 673, A26, doi: [10.1051/0004-6361/202243681](https://doi.org/10.1051/0004-6361/202243681)
- Grier, C. J., Peterson, B. M., Pogge, R. W., et al. 2012, ApJL, 744, L4, doi: [10.1088/2041-8205/744/1/L4](https://doi.org/10.1088/2041-8205/744/1/L4)
- Grupe, D., Komossa, S., & Gallo, L. C. 2007, ApJL, 668, L111, doi: [10.1086/523042](https://doi.org/10.1086/523042)
- Grupe, D., Komossa, S., Gallo, L. C., et al. 2008, ApJ, 681, 982, doi: [10.1086/588213](https://doi.org/10.1086/588213)
- Grupe, D., Komossa, S., Gallo, L. C., et al. 2012, ApJS, 199, 28, doi: [10.1088/0067-0049/199/2/28](https://doi.org/10.1088/0067-0049/199/2/28)
- Harrison, F. A., Craig, W. W., Christensen, F. E., et al. 2013, ApJ, 770, 103, doi: [10.1088/0004-637X/770/2/103](https://doi.org/10.1088/0004-637X/770/2/103)
- Hell, N., Brown, G. V., Eckart, M. E., et al. 2025, arXiv e-prints, arXiv:2506.17106, doi: [10.48550/arXiv.2506.17106](https://doi.org/10.48550/arXiv.2506.17106)
- HI4PI Collaboration, Ben Bekhti, N., Flöer, L., et al. 2016, A&A, 594, A116, doi: [10.1051/0004-6361/201629178](https://doi.org/10.1051/0004-6361/201629178)
- Holzner, T., Behar, E., & Kaspi, S. 2007, ApJ, 663, 799, doi: [10.1086/518416](https://doi.org/10.1086/518416)
- Hopkins, P. F., & Elvis, M. 2010, MNRAS, 401, 7, doi: [10.1111/j.1365-2966.2009.15643.x](https://doi.org/10.1111/j.1365-2966.2009.15643.x)
- Kaastra, J. S., & Bleeker, J. A. M. 2016, A&A, 587, A151, doi: [10.1051/0004-6361/201527395](https://doi.org/10.1051/0004-6361/201527395)
- Kaastra, J. S., Mewe, R., & Nieuwenhuijzen, H. 1996, in UV and X-ray Spectroscopy of Astrophysical and Laboratory Plasmas, ed. K. Yamashita & T. Watanabe, 411–414
- Kaastra, J. S., Paerels, F. B. S., Durret, F., Schindler, S., & Richter, P. 2008, SSRv, 134, 155, doi: [10.1007/s11214-008-9310-y](https://doi.org/10.1007/s11214-008-9310-y)
- Kaastra, J. S., Raassen, A. J. J., de Plaa, J., & Gu, L. 2020, SPEX X-ray spectral fitting package, 3.06.00 Zenodo, doi: [10.5281/zenodo.3939056](https://doi.org/10.5281/zenodo.3939056)
- Kaastra, J. S., Kriss, G. A., Cappi, M., et al. 2014, Science, 345, 64, doi: [10.1126/science.1253787](https://doi.org/10.1126/science.1253787)
- Kara, E., Alston, W. N., Fabian, A. C., et al. 2016, MNRAS, 462, 511, doi: [10.1093/mnras/stw1695](https://doi.org/10.1093/mnras/stw1695)
- Kara, E., & García, J. 2025, ARA&A, 63, 379, doi: [10.1146/annurev-astro-071221-052844](https://doi.org/10.1146/annurev-astro-071221-052844)
- Kara, E., Mehdipour, M., Kriss, G. A., et al. 2021, ApJ, 922, 151, doi: [10.3847/1538-4357/ac2159](https://doi.org/10.3847/1538-4357/ac2159)
- Keek, L., & Ballantyne, D. R. 2016, MNRAS, 456, 2722, doi: [10.1093/mnras/stv2882](https://doi.org/10.1093/mnras/stv2882)
- Kinney, A. L., Calzetti, D., Bohlin, R. C., et al. 1996, ApJ, 467, 38, doi: [10.1086/177583](https://doi.org/10.1086/177583)
- Komossa, S., Grupe, D., Gallo, L. C., et al. 2020, A&A, 643, L7, doi: [10.1051/0004-6361/202039098](https://doi.org/10.1051/0004-6361/202039098)
- Komossa, S., Grupe, D., Marziani, P., et al. 2026, Advances in Space Research, 77, 4041, doi: [10.1016/j.asr.2025.04.058](https://doi.org/10.1016/j.asr.2025.04.058)
- Kriss, G. A., De Rosa, G., Ely, J., et al. 2019, ApJ, 881, 153, doi: [10.3847/1538-4357/ab3049](https://doi.org/10.3847/1538-4357/ab3049)
- Krolik, J. H., McKee, C. F., & Tarter, C. B. 1981, ApJ, 249, 422, doi: [10.1086/159303](https://doi.org/10.1086/159303)
- Laha, S., Guainazzi, M., Dewangan, G. C., Chakravorty, S., & Kembhavi, A. K. 2014, MNRAS, 441, 2613, doi: [10.1093/mnras/stu669](https://doi.org/10.1093/mnras/stu669)
- Laha, S., Reynolds, C. S., Reeves, J., et al. 2021, Nature Astronomy, 5, 13, doi: [10.1038/s41550-020-01255-2](https://doi.org/10.1038/s41550-020-01255-2)
- Leighly, K. M., Cooper, E., Grupe, D., Terndrup, D. M., & Komossa, S. 2015, ApJL, 809, L13, doi: [10.1088/2041-8205/809/1/L13](https://doi.org/10.1088/2041-8205/809/1/L13)
- Leighly, K. M., Hamann, F., Casebeer, D. A., & Grupe, D. 2009, ApJ, 701, 176, doi: [10.1088/0004-637X/701/1/176](https://doi.org/10.1088/0004-637X/701/1/176)
- Liu, H., Parker, M. L., Jiang, J., et al. 2021, MNRAS, 506, 5190, doi: [10.1093/mnras/stab2033](https://doi.org/10.1093/mnras/stab2033)
- Lodders, K., Palme, H., & Gail, H.-P. 2009, Landolt Börnstein, doi: [10.1007/978-3-540-88055-4_34](https://doi.org/10.1007/978-3-540-88055-4_34)
- Longinotti, A. L., Krongold, Y., Guainazzi, M., et al. 2015, ApJL, 813, L39, doi: [10.1088/2041-8205/813/2/L39](https://doi.org/10.1088/2041-8205/813/2/L39)
- Longinotti, A. L., Nucita, A., Santos-Lleo, M., & Guainazzi, M. 2008, A&A, 484, 311, doi: [10.1051/0004-6361:200809374](https://doi.org/10.1051/0004-6361:200809374)
- Longinotti, A. L., Krongold, Y., Kriss, G. A., et al. 2013, ApJ, 766, 104, doi: [10.1088/0004-637X/766/2/104](https://doi.org/10.1088/0004-637X/766/2/104)
- Longinotti, A. L., Kriss, G., Krongold, Y., et al. 2019, ApJ, 875, 150, doi: [10.3847/1538-4357/ab125a](https://doi.org/10.3847/1538-4357/ab125a)
- Magdziarz, P., & Zdziarski, A. A. 1995, MNRAS, 273, 837, doi: [10.1093/mnras/273.3.837](https://doi.org/10.1093/mnras/273.3.837)
- Mao, J., Kriss, G. A., Landt, H., et al. 2022a, ApJ, 940, 41, doi: [10.3847/1538-4357/ac99de](https://doi.org/10.3847/1538-4357/ac99de)
- Mao, J., Kaastra, J. S., Mehdipour, M., et al. 2022b, arXiv e-prints, arXiv:2204.06813, <https://arxiv.org/abs/2204.06813>
- Markowitz, A. G., Krumpe, M., & Nikutta, R. 2014, MNRAS, 439, 1403, doi: [10.1093/mnras/stt2492](https://doi.org/10.1093/mnras/stt2492)
- Mason, K. O., Breeveld, A., Much, R., et al. 2001, A&A, 365, L36, doi: [10.1051/0004-6361:20000044](https://doi.org/10.1051/0004-6361:20000044)

- Matamoro Zatarain, T., Costantini, E., Juráňová, A., & Rogantini, D. 2025, *A&A*, 696, A50, doi: [10.1051/0004-6361/202451710](https://doi.org/10.1051/0004-6361/202451710)
- Mehdipour, M., Kaastra, J. S., & Kallman, T. 2016, *A&A*, 596, A65, doi: [10.1051/0004-6361/201628721](https://doi.org/10.1051/0004-6361/201628721)
- Mehdipour, M., Kriss, G. A., Costantini, E., et al. 2022, *ApJL*, 934, L24, doi: [10.3847/2041-8213/ac822f](https://doi.org/10.3847/2041-8213/ac822f)
- Mehdipour, M., Kaastra, J. S., Kriss, G. A., et al. 2015, *A&A*, 575, A22, doi: [10.1051/0004-6361/201425373](https://doi.org/10.1051/0004-6361/201425373)
- Mehdipour, M., Kaastra, J. S., Costantini, E., et al. 2018, *A&A*, 615, A72, doi: [10.1051/0004-6361/201832604](https://doi.org/10.1051/0004-6361/201832604)
- Mehdipour, M., Kriss, G. A., Kaastra, J. S., et al. 2021, *arXiv e-prints*, arXiv:2106.14957, <https://arxiv.org/abs/2106.14957>
- Miller, J. M., Kaastra, J. S., Miller, M. C., et al. 2015, *Nature*, 526, 542, doi: [10.1038/nature15708](https://doi.org/10.1038/nature15708)
- Miller, J. M., Zoghbi, A., Reynolds, M. T., et al. 2021, *ApJL*, 911, L12, doi: [10.3847/2041-8213/abeff6](https://doi.org/10.3847/2041-8213/abeff6)
- O'Donnell, J. E. 1994, *ApJ*, 422, 158, doi: [10.1086/173713](https://doi.org/10.1086/173713)
- Ogorzalek, A., King, A. L., Allen, S. W., Raymond, J. C., & Wilkins, D. R. 2022, *MNRAS*, 516, 5027, doi: [10.1093/mnras/stac2389](https://doi.org/10.1093/mnras/stac2389)
- O'Neill, P. M., Nandra, K., Cappi, M., Longinotti, A. L., & Sim, S. A. 2007, *MNRAS*, 381, L94, doi: [10.1111/j.1745-3933.2007.00376.x](https://doi.org/10.1111/j.1745-3933.2007.00376.x)
- Parker, M. L., Wilkins, D. R., Fabian, A. C., et al. 2014, *MNRAS*, 443, 1723, doi: [10.1093/mnras/stu1246](https://doi.org/10.1093/mnras/stu1246)
- Parker, M. L., Longinotti, A. L., Schartel, N., et al. 2019, *MNRAS*, 490, 683, doi: [10.1093/mnras/stz2566](https://doi.org/10.1093/mnras/stz2566)
- Partington, E. R., Cackett, E. M., Kara, E., et al. 2023, *ApJ*, 947, 2, doi: [10.3847/1538-4357/acbf44](https://doi.org/10.3847/1538-4357/acbf44)
- Petrucci, P. O., Ursini, F., De Rosa, A., et al. 2018, *A&A*, 611, A59, doi: [10.1051/0004-6361/201731580](https://doi.org/10.1051/0004-6361/201731580)
- Ponti, G., Papadakis, I., Bianchi, S., et al. 2012, *A&A*, 542, A83, doi: [10.1051/0004-6361/201118326](https://doi.org/10.1051/0004-6361/201118326)
- Poole, T. S., Breeveld, A. A., Page, M. J., et al. 2008, *MNRAS*, 383, 627, doi: [10.1111/j.1365-2966.2007.12563.x](https://doi.org/10.1111/j.1365-2966.2007.12563.x)
- Pothier-Bogoslowski, L. K., Gallo, L. C., Gonzalez, A. G., Buhariwalla, M. Z., & Miller, J. M. 2025, *MNRAS*, 540, 3468, doi: [10.1093/mnras/staf940](https://doi.org/10.1093/mnras/staf940)
- Pottie, B., Gallo, L. C., Gonzalez, A. G., & Miller, J. M. 2023, *MNRAS*, 525, 3633, doi: [10.1093/mnras/stad2449](https://doi.org/10.1093/mnras/stad2449)
- Pounds, K. A., Stanger, V. J., Turner, T. J., King, A. R., & Czerny, B. 1987, *MNRAS*, 224, 443, doi: [10.1093/mnras/224.2.443](https://doi.org/10.1093/mnras/224.2.443)
- Rogantini, D., Costantini, E., Gallo, L. C., et al. 2022a, *MNRAS*, doi: [10.1093/mnras/stac2552](https://doi.org/10.1093/mnras/stac2552)
- Rogantini, D., Mehdipour, M., Kaastra, J., et al. 2022b, *ApJ*, 940, 122, doi: [10.3847/1538-4357/ac9c01](https://doi.org/10.3847/1538-4357/ac9c01)
- Roming, P. W. A., Kennedy, T. E., Mason, K. O., et al. 2005, *SSRv*, 120, 95, doi: [10.1007/s11214-005-5095-4](https://doi.org/10.1007/s11214-005-5095-4)
- Schlafly, E. F., & Finkbeiner, D. P. 2011, *ApJ*, 737, 103, doi: [10.1088/0004-637X/737/2/103](https://doi.org/10.1088/0004-637X/737/2/103)
- Serafinelli, R., Braito, V., Severgnini, P., et al. 2021, *A&A*, 654, A32, doi: [10.1051/0004-6361/202141474](https://doi.org/10.1051/0004-6361/202141474)
- Shakura, N. I., & Sunyaev, R. A. 1973, in *IAU Symposium*, Vol. 55, X- and Gamma-Ray Astronomy, ed. H. Bradt & R. Giacconi, 155
- Strüder, L., Briel, U., Dennerl, K., et al. 2001, *A&A*, 365, L18, doi: [10.1051/0004-6361:20000066](https://doi.org/10.1051/0004-6361:20000066)
- Tananbaum, H., Peters, G., Forman, W., et al. 1978, *ApJ*, 223, 74, doi: [10.1086/156236](https://doi.org/10.1086/156236)
- Tarter, C. B., Tucker, W. H., & Salpeter, E. E. 1969, *ApJ*, 156, 943, doi: [10.1086/150026](https://doi.org/10.1086/150026)
- Tashiro, M., Kelley, R., Watanabe, S., et al. 2025, *PASJ*, doi: [10.1093/pasj/psaf023](https://doi.org/10.1093/pasj/psaf023)
- Titarchuk, L. 1994, *ApJ*, 434, 570, doi: [10.1086/174760](https://doi.org/10.1086/174760)
- Tombesi, F., Cappi, M., Reeves, J. N., et al. 2010, *A&A*, 521, A57, doi: [10.1051/0004-6361/200913440](https://doi.org/10.1051/0004-6361/200913440)
- Tripathi, S., McGrath, K. M., Gallo, L. C., et al. 2020, *MNRAS*, 499, 1266, doi: [10.1093/mnras/staa2817](https://doi.org/10.1093/mnras/staa2817)
- Turner, T. J., Nandra, K., Zdziarski, A. A., et al. 1993, *ApJ*, 407, 556, doi: [10.1086/172537](https://doi.org/10.1086/172537)
- Wang, Y., Kaastra, J., Mehdipour, M., et al. 2022, *A&A*, 657, A77, doi: [10.1051/0004-6361/202141599](https://doi.org/10.1051/0004-6361/202141599)
- Wilkins, D. R., & Gallo, L. C. 2015, *MNRAS*, 449, 129, doi: [10.1093/mnras/stv162](https://doi.org/10.1093/mnras/stv162)
- Wilkins, D. R., Gallo, L. C., Costantini, E., Brandt, W. N., & Blandford, R. D. 2022, *MNRAS*, 512, 761, doi: [10.1093/mnras/stac416](https://doi.org/10.1093/mnras/stac416)
- Wilkins, D. R., Gallo, L. C., Grupe, D., et al. 2015, *MNRAS*, 454, 4440, doi: [10.1093/mnras/stv2130](https://doi.org/10.1093/mnras/stv2130)
- Xiang, X., Miller, J. M., Behar, E., et al. 2025, *ApJL*, 988, L54, doi: [10.3847/2041-8213/adee9b](https://doi.org/10.3847/2041-8213/adee9b)
- Xu, Y., Pinto, C., Rogantini, D., et al. 2023, *MNRAS*, 523, 2158, doi: [10.1093/mnras/stad1565](https://doi.org/10.1093/mnras/stad1565)
- Xu, Y., Pinto, C., Rogantini, D., et al. 2024, *A&A*, 687, A179, doi: [10.1051/0004-6361/202349001](https://doi.org/10.1051/0004-6361/202349001)
- Zaidouni, F., Kara, E., Kosec, P., et al. 2024, *ApJ*, 974, 91, doi: [10.3847/1538-4357/ad6771](https://doi.org/10.3847/1538-4357/ad6771)
- Zycki, P. T., & Czerny, B. 1994, *MNRAS*, 266, 653, doi: [10.1093/mnras/266.3.653](https://doi.org/10.1093/mnras/266.3.653)

APPENDIX

A. APPENDIX INFORMATION

Figure 10 provides a visual summary of the short-timescale spectral variability discussed in the main text. We display the time evolution of the RGS spectra in the Fe XVII–O VIII band (14.8–19.2 Å), where the variability is most apparent. Each panel shows one epoch fitted independently (RGS1 and RGS2 fitted simultaneously), with the best-fit model overplotted. The depth of the O VIII Ly α absorption and the strength/shape of the Fe UTA change markedly from epoch to epoch, providing a direct, model-independent view of the evolving wind transmission over the ~ 8 days of the campaign.

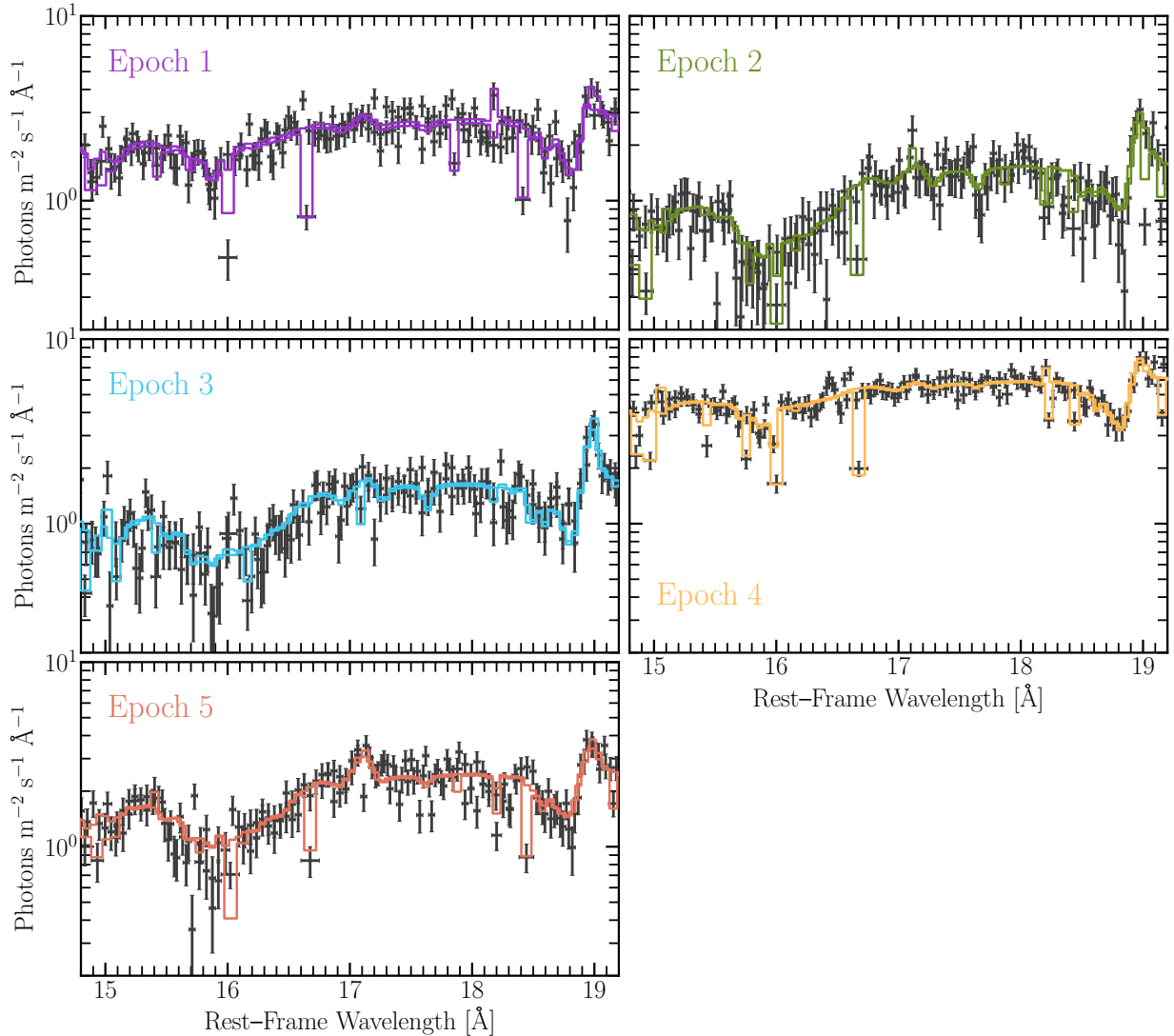


Figure 10. Time evolution of the XMM-Newton/RGS spectra of Mrk 335 in the 14.8–19.2 Å rest-frame band (Fe XVII–O VIII). Each panel shows one epoch (Epochs 1–5), with RGS1 and RGS2 fitted simultaneously; the best-fit model is overplotted. Colors correspond to the epochs and match the palette used in the light-curve figures. The spectra illustrate strong variability in the soft X-ray band, including changes in the continuum level and in the depth/shape of the O VIII Ly α absorption and Fe UTA features over the ~ 8 -day campaign.